GEOMETRY OF THE DOLPO-MUGU FOLDS: IMPLICATIONS FOR THE DEEP CRUSTAL STRUCTURE OF CENTRAL NEPAL

A Thesis

Presented to

the Faculty of the Department of Earth and Atmospheric Science

University of Houston

In Partial Fulfillment of the Requirements for the Degree

Master of Science

By

James K. Stutz

May 2012

GEOMETRY OF THE DOLPO-MUGU FOLDS: IMPLICATIONS FOR THE DEEP CRUSTAL STRUCTURE OF CENTRAL NEPAL

_____

James K. Stutz

Approved:

_____

Dr. Michael Murphy, Chairman

_____

Dr. Alex Robinson

_____

Dr. Alex Webb

_____

Dr. Mark A. Smith
Dean, College of Natural Sciences and Mathematics

ACKNOWLEDGEMENTS

I'd like to first thank my wife Megan whose patience, support, and encouragement have been unwavering throughout the duration of this project. I'd also like to thank my son William for allowing his father to spend many hours at the office. I am also grateful to my parents who taught me the importance of education and hard work, and who inspired in me a curiosity about the world. I'd like to thank Dr. Michael Murphy for his help and mentorship in the development of this project; this could not have been completed without him. I also want to thank Dr. Alex Robinson and Dr. Alex Webb for their comments and feedback. Finally, I 'd like to thank the many other family and friends who have supported me in my efforts.

GEOMETRY OF THE DOLPO-MUGU FOLDS: IMPLICATIONS FOR THE DEEP CRUSTAL STRUCTURE OF CENTRAL NEPAL

An Abstract of a Thesis

Presented to

the Faculty of the Department of Earth and Atmospheric Sciences

University of Houston

In Partial Fulfillment

of the Requirements for the Degree

Master of Science

By

James K. Stutz

May 2012

Abstract:

Current shortening calculations (700-300 km) across the strike of the Himalayan orogen are significantly less than what has been predicted by plate reconstruction models and other regional studies (1200-800 km). This study investigates a region in the High Himalaya of western Nepal that contains shortening structures not currently accounted for in shortening budgets within the thrust belt. The first-order structures in the study area are a synclinorium and anticlinorium defined by the contact, -- the South Tibetan Detachment (STD) -- between two main tectonostratigraphic units: the Tethyan Himalayan sequence (THS) and the Greater Himalayan Crystallines (GHC). Because the STD is interpreted to have ceased movement ca. 19 Ma, the timing for these folds is bracketed between ~19 Ma and ~11 Ma. A new geologic map is constructed by compiling previous maps and serves as the foundation for structural analysis. These folds can be traced for ~150 km in an east-west direction. Cross sections, structure contour maps, and stereoplots of the STD show an amplitude of ~9km with a shallow plunge to the SE.

Three hypotheses for thrust belt architecture below the anticlinorium are considered. These are (A) a duplex, (B) a fault-bend fold and (C) a blind thrust. Each of these models makes predictions of horizontal shortening. The duplex hypothesis predicts ~33 km of horizontal shortening, the fault-bend fold model predicts ~25 km of shortening, and the blind thrust model predicts ~8 km of shortening. Based on geometry and structural position I correlate the Dolpo-Mugu folds with similar folds to the east and west along the strike of the orogen; the Gurla Mandhata Crystalline complex is ~150 km to the west of Dolpo-Mugu, and the Manaslu folds are ~200 km to the east for a cumulative along strike axis of 350 km. These models predict vertical thickening within the GHC in contrast to previous models that show constant thickness in this region of the Himalaya.

TABLE OF CONTENTS

1. INTRODUCTION

The Himalayan orogen, produced from the convergence of the Indian sub-continent with Eurasia, is considered the paradigm for continent-continent collision. With its towering peaks and an along-strike trace of over 2500 km the orogenic belt provides an opportunity to explore fault geometries, kinematics, and shortening budgets in an active convergent zone. Studies on the Himalayan orogen indicate that approximately 2500 km of Cenozoic convergence has occurred between Asia and India since collision at ~50 Ma (Achache et al., 1984; Patriat and Achache, 1984; Besse et al., 1984; Besse and Courtillot, 1988). Recent GPS studies, regional structural studies, and mass balance calculations suggest that approximately one third to one half of that convergence can be accounted for by crustal shortening along the fold-thrust belt (Le Pichon et al., 1992). This predicts 800-1200 km of shortening along strike. However, actual minimum estimates for shortening range from >280 km in eastern Nepal (Schelling, 1992), ~400-500 km in western Nepal (Robinson, 2006), ~470 km in Pakistan (Coward and Butler, 1985) and >700 km in northern India (Srivastava and Mitra, 1994). The discrepancy between predicted and observed shortening presents a challenge to current understandings of the development of the Himalayan orogen.

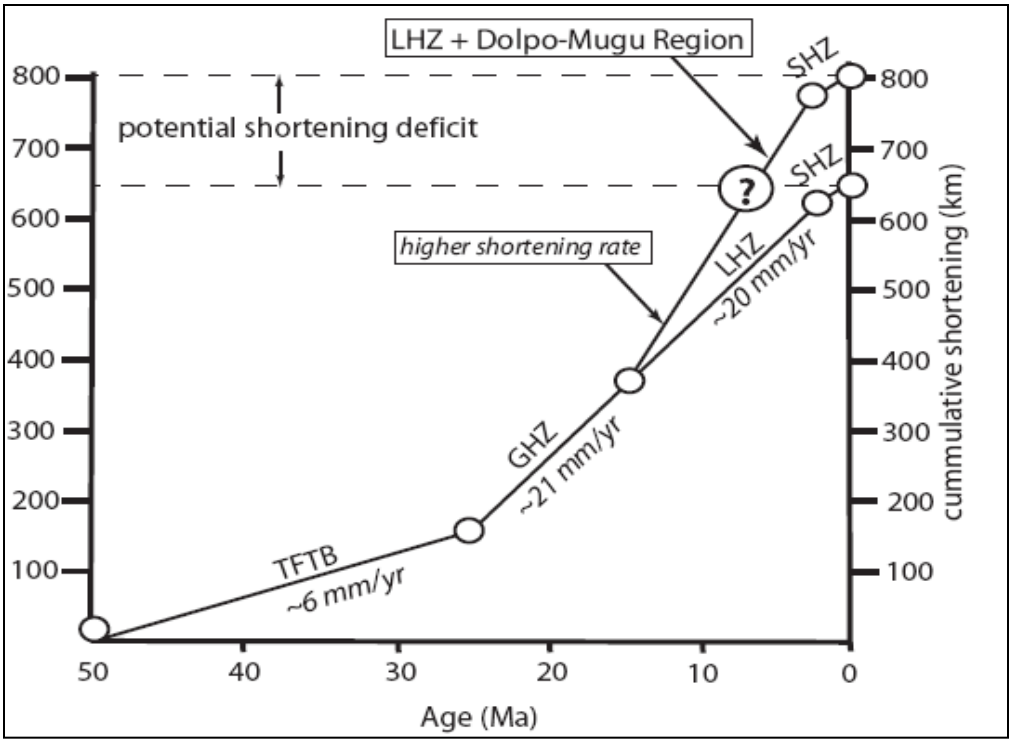

Figure 1. From Murphy (2011) based on data compiled by Decelles et al.,1998.

Approximate shortening budgets for major shortening events of the Himalayan orogen are represented in figure 1 (Murphy, 2011). Currently ~650 km of shortening can be accounted for by these units, but a shortening deficit exists according to regional studies (Le Pichon et al., 1992) which predict upwards of 800-1200 km of shortening as discussed above. In the high Himalaya of the Dolpo-Mugu region of west-central Nepal there is a large antiform/synform pair that has hitherto not been integrated into regional shortening estimates (figure 2). The shortening accommodated by this structure may contribute to closing the gap between predicted and observed shortening calculations.

In the 1960's and 1970's Austrian scientist Gerhard Fuchs explored this region of central-west Nepal and produced a detailed geologic map of the synclinorium (Fuchs 1977). Many advancement have since been made in the overall understanding of the nature of Himalayan thrust belt such as the identification of the South Tibetan Detachment zone which spans the length of the central Himalaya including the Dolpo-Mugu area. This study will build on Fuchs' early work in this region and bring it into the 21st century.

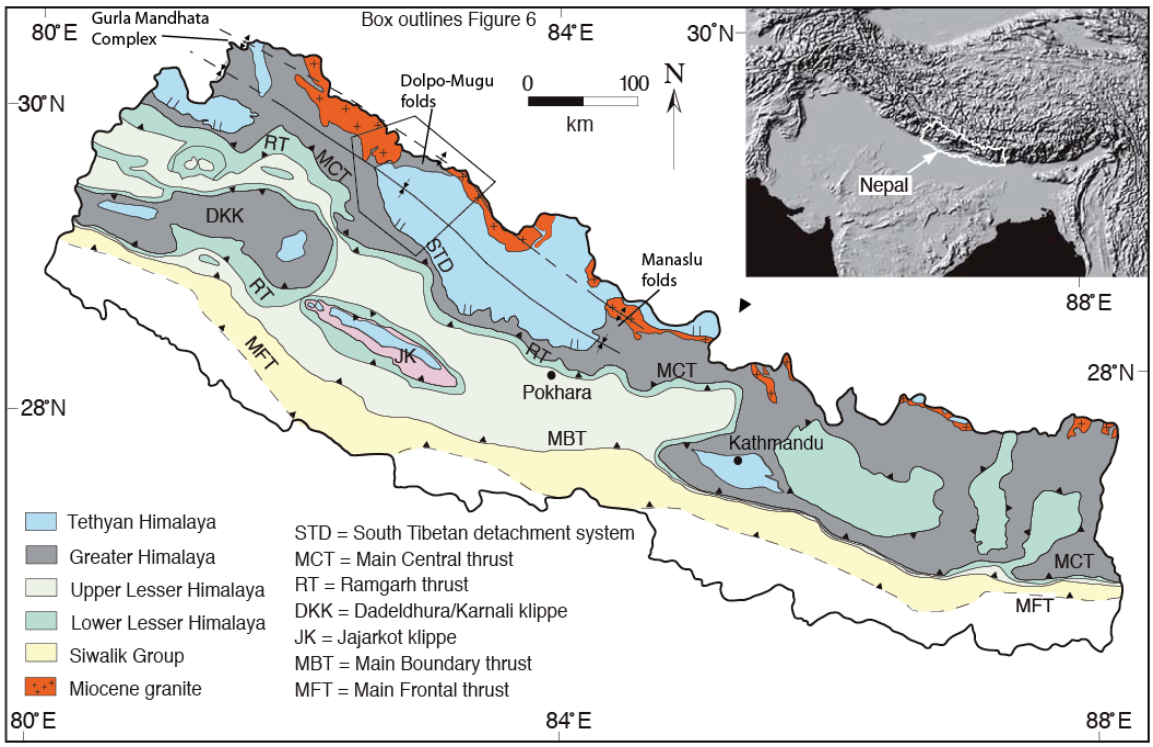

Figure 2. Tectnostratigraphic map of Nepal modified from Robinson, 2008. Box outlines field area of Fuchs, 1977. Gurla Mandhata core complex and Manaslu folds are also highlighted for reference.

2. REGIONAL GEOLOGY

2.1 Regional Fault Systems

The Himalayan orogenic belt evolved during the Cenozoic collision of the Indian continent with the Eurasian plate beginning at approximately 55-50 Ma. The resultant fold-thrust belt which developed is characterized by major strike-parallel lithotectonic units which are bounded by north-dipping fault systems. From south to north these fault systems are the Main Frontal Thrust (MFT), the Main Boundary Thrust (MBT), the Main Central Thrust (MCT), and the South Tibetan Detachment (STD) (figures 2 & 3).

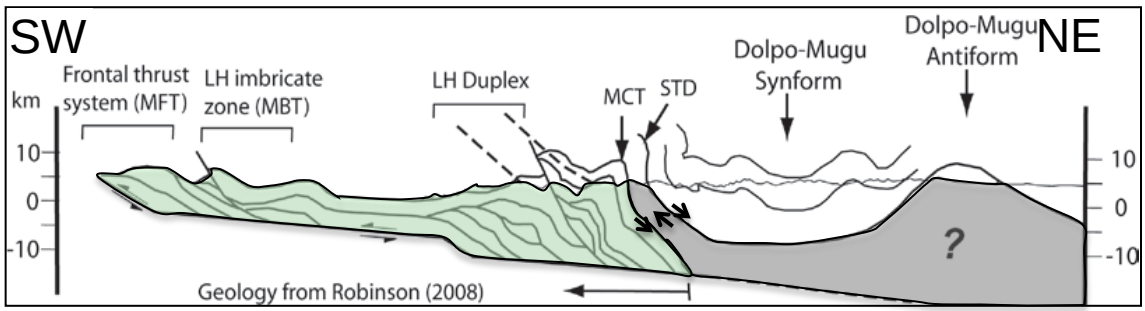

Figure 3. Major lithotectonic units and fault zones. The LHS is toward the SW, followed by the GHS and THS toward the NE respectively. Adapted from Robinson, 2008.

2.1.1 Lesser Himalayan Sequence

The structurally lowest lithotectonic unit is the Lesser Himalayan Sequence (LHS), which is bounded below by the MBT and above by the MCT. The LHS lies primarily along the foothills of the Himalaya and is generally poorly exposed. It consists of lower-greenschist to lower-amphibolite-facies clastic metasedimentary units. The LHS has a structurally complex system of fold-and-thrust nappes (Hodges, 2000), and the cumulative stratigraphic thickness is approximately 8-10 km.

2.1.2 Greater Himalayan Crystalline complex

The Greater Himalayan Crystalline complex (GHC) is structurally above the LHS and is bounded above by the STD. The GHC is primarily high-grade meta-sedimentary and meta-igneous rocks (Hodges, 2000). Following the classification scheme of Le Fort (1975), the GHC is subdivided into three successive units referred to as Formation I, II, and III. At the base of the GHC Formation I consists predominantly of biotite-muscovite gneiss and ranges widely in thickness throughout the Himalayan orogen (Hodges, 2000). In western Nepal Formation I is ~6 km thick (Robinson, 2006). Above Formation I, Formation II is predominantly composed of banded calc-silicate gneiss and in central Nepal is approximately 2-4 km thick, though in several central Himalayan areas this unit is entirely absent (Robinson, 2006). The upper most section is Formation III is a nearly homogeneous augen orthogneiss that can be traced continuously from eastern to central Nepal. It is approximately 300 m thick (Hodges, 2000). The upper sections of the GHC contain intruded late Oligocene to middle Miocene leucogranites (Robinson et al., 2006). Those will be discussed in more detail below.

2.1.3 Tethyan Himalayan Sequence

The Tethyan Sedimentary Sequence (THS) is a nearly complete Paleozoic to Mesozoic stratigraphic record of the northern continental margin of the paleo-Indian sub-continent before collision with Eurasia. It is well exposed throughout the Dolpo-Mugu synclinorium and is ~7000 meter thick (Hodges 2000). Structurally above the STD, the THS is predominantly unmetamorphosed strata, although some low-grade metasedimentary units can be found at its base. Its units can be subdivided into Paleozoic and Mesozoic components. Paleozoic units are composed of quartzites, calc-silicates, quartz sandstone, minor limestones and dolostone, and are ~5.2-6.0 km thick. The Mesozoic units are composed of fossiliferous and silty limestone, and interbedded sandstone and shale. These unit are ~ 3.3-4.4 km thick. (Murphy and Yin, 2003).

2.2 South Tibetan Detachment System and Main Central Thrust

The South Tibetan Detachment (STD) zone has traditionally been interpreted as a system of top-to-the-north normal faults that extend across the length of the Himalayan thrust belt. However, some models describe the STD as a passive roof thrust in which the THS remains relatively stationary while the underlying GHC propagates forward (Webb, 2007). The STD is the contact between two major Himalayan lithotectonic domains; the sedimentary and meta-sedimentary rocks of the structurally higher Tethyan Himalayan Sequence (THS), and the structurally lower Greater Himalayan Crystalline complex (GHC). The STD juxtaposes the

low-grade metasedimentary rocks of the THS in the hanging wall against amphibolite-facies gneisses of the GHC in the footwall (Hodges, 2000). Shear sense indicators have suggested both a normal top-to-the-north sense of shear as well as reverse top-to-the-south sense of shear (Webb et al., 2007), suggesting that the STD has a history of reversals in shear sense. It has been suggested that the STD had an early thrust component (Weismayr & Grasemann, 2002) that has been overprinted by several phases of normal, reverse, and possibly strike-slip sense motion (Godin et al., 1999). However, these observations may be best accounted for by a tectonic wedge model for GHC extrusion which will be discussed below. A minimum estimate of 35 km of slip for the STD has been suggested (Birchfield et al. 1992). The STD consists of a complex zone of multiple strands that may have operated at different times and under different mechanical conditions (plastic to brittle) (Godin et al., 2006). Timing estimates for the STD indicate that it ceased moving at ca. 19-16 Ma (Searle and Godin, 2003; Godin et al., 2006; Gleeson & Godin, 2005) which implies that the Dolpo-Mugu synclinorium and anticlinorium developed after or during the early Miocene.

At the base of the GHC the Main Central Thrust (MCT) system defines the contact between the GHC and the Lesser Himalayan Sedimentary sequence (LHS) below. With top-to-the-north normal sense shear of the STD which bounds the top of the GHC, and top-to-the-south reverse sense shear along the bottom at the MCT, the GHC has been described, through various competing models, as having been extruded from mid-crustal levels. GHC extrusion probably ceased by ~19 Ma

according to dating of latest slip on the STD in central Nepal (Gleeson and Godin, 2006).

2.3 Deformation History

Crustal thickening of the THS predominantly occurred during Eocene-Oligocene time (Godin et al., 1999; Godin et al., 2001; Lee et al., 2000; Aoya et al., 2005; Kellet and Godin, 2009; Aikman et al., 2008). This activity induced metamorphism and anatectic melting within the GHC (Godin et al., 2006; Aoya et al., 2005; Lee and Whitehouse, 2007; Larson et al., 2010), which is associated with numerous leucogranites along the upper portions of the GHC. Furthermore, this thickening is also interpreted to be associated with early Miocene initiation of normal sense slip along the STD (top-to-north) and thrust sense slip along the MCT (top-to-south), resulting in displacement of GHC toward the foreland. Large-scale folding of the STD and adjacent lithotectonic packages began after cessation of STD slip, but before extensional faulting in the Thakkola graben which cross-cut the folds ca. 11 Ma (Garzione et al., 2003), bracketing folding of the STD to within 19-11 Ma.

2.4 Kinematic Models of GHC Extrusion

There have been a number of models put forth to explain the relationship between the STD and the MCT and the kinematics of GHC extrusion. These models can largely be summarized by two end-member hypotheses.

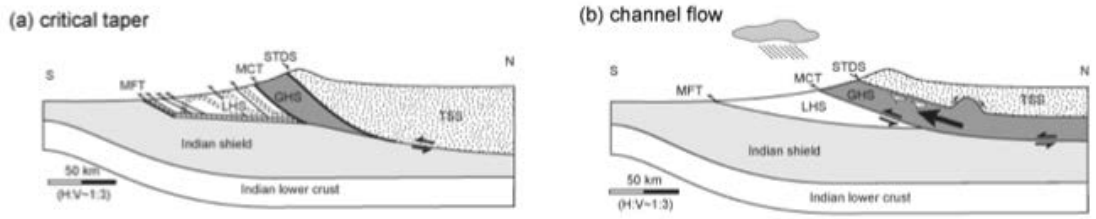

Figure 4. Models of GHC extrusion (a) critical taper (Robinson et al., 2006; Kohn, 2008); (b) channel flow (Beaumont et al., 2001; Jamieson et al., 2004).

The first is the channel flow model (Bird, 1991; Grujic et al., 1996; Beaumont et al., 2001; 2004; 2006) in which the GHC at mid-crustal levels is significantly less viscous than bounding lithotectonic units. The over-thickened crust below Tibet and the thinner sub-India crust create a lithostatic pressure gradient to which the GHC reacts by lateral flow towards a rapidly eroding southern boundary (figure 4a).

The second end-member model is the critical taper wedge model in which the GHC is translated and deformed in the hanging wall of a thrust that has propagated in order to thicken the Himalayan orogenic wedge in response to a taper angle that is less than the critical taper angle (Kohn, 2008) (figure 4b).

An alternative model for GHC extrusion is the tectonic wedge model (Price, 1986; Yin, 2006; Webb et al., 2007). This model interprets the GHC as a tectonic

wedge in which the STD branches off of the MCT at the foreland point of the wedge where it tapers out (figure 5).

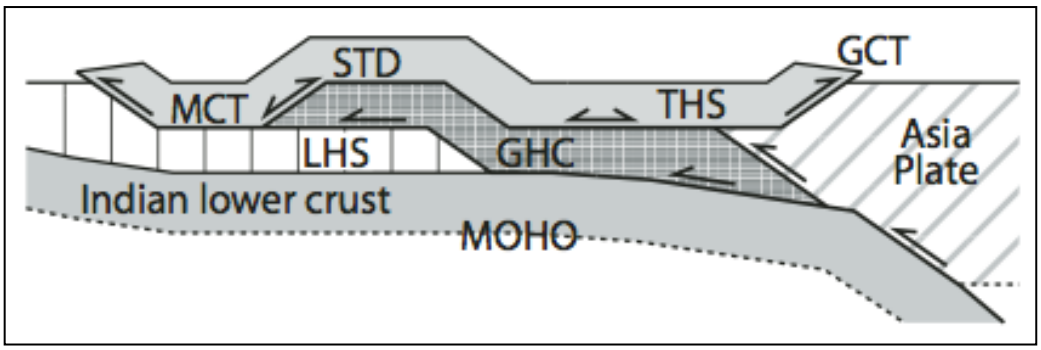

Figure 5. Schematic diagram of the tectonic wedge model of GHC extrusion. Adapted from Webb et al., 2007.

The STD has been mapped westward into the Rhotang La area of north India where it was observed to merge with the MCT defining a branch line of a southward-tapering GHC wedge (Webb et al., 2007; Yin, 2006). Other models of GHC extrusion do not predict this relationship between the STD and MCT. Shear-sense indicators in the STD in northern India were also observed to show both normal sense and thrust sense motion. In this model top-to-the-south shear-sense indicators in the STD are interpreted to be records from the MCT hanging-wall forward of the MCT-STD branch line that have been transported through the branch line and into the hanging-wall (hinterward) of the STD as the GHC wedge propagates forwards (Webb et al., 2007). These alternating shear-sense fabrics are inconsistent with a channel flow model which predict only normal shear-sense indicators in the hanging-wall of the STD. Channel flow models also require slip on the STD and MCT to cease at their branch line, but there is evidence of >100 km of

MCT slip in the region of the branch line which is inconsistent with channel flow (Webb, 2007).

3. STRATIGRAPHY AND TECTONOSTRATIGRAPHY OF DOLPO-MUGU FOLDS

The Dolpo and Mugu districts in Nepal contain exposures of a pair of regional scale folds (Fuchs, 1964; Fuchs, 1977) that are defined by the STD; the contact between the GHS and the THS (figure 6).

3.1 Tethyan Stratigraphy

In the western Dolpo and eastern Mugu regions of central-west Nepal the THS contains deposits from the Cambrian to the Jurassic (Fuchs 1977) (figure 7). The THS lies in structural contact above the Greater Himalayan Sequence along the South Tibetan Detachment system.

Dhaulagiri Carbonate

At the base of the THS lies the 3-4 km thick Dhaulagiri metamorphic carbonate and limestone sequence. It has been suggested that the incredible thickness is due to subsidence at time of deposition coupled with rapid sediment deposition (Fuchs 1977). Based on fossil evidence the Dhaulagiri formation is primarily Ordovician age, making it broadly correlative with the Nilgiri limestone of the Annapurna region, although the possibility remains that its lower portions are Cambrian in age (Fuchs 1977). The lower portions of the sequence are described as a metamorphic carbonate series with banded calc-silicate marbles, grey medium to course-grained marbles, fine-grained

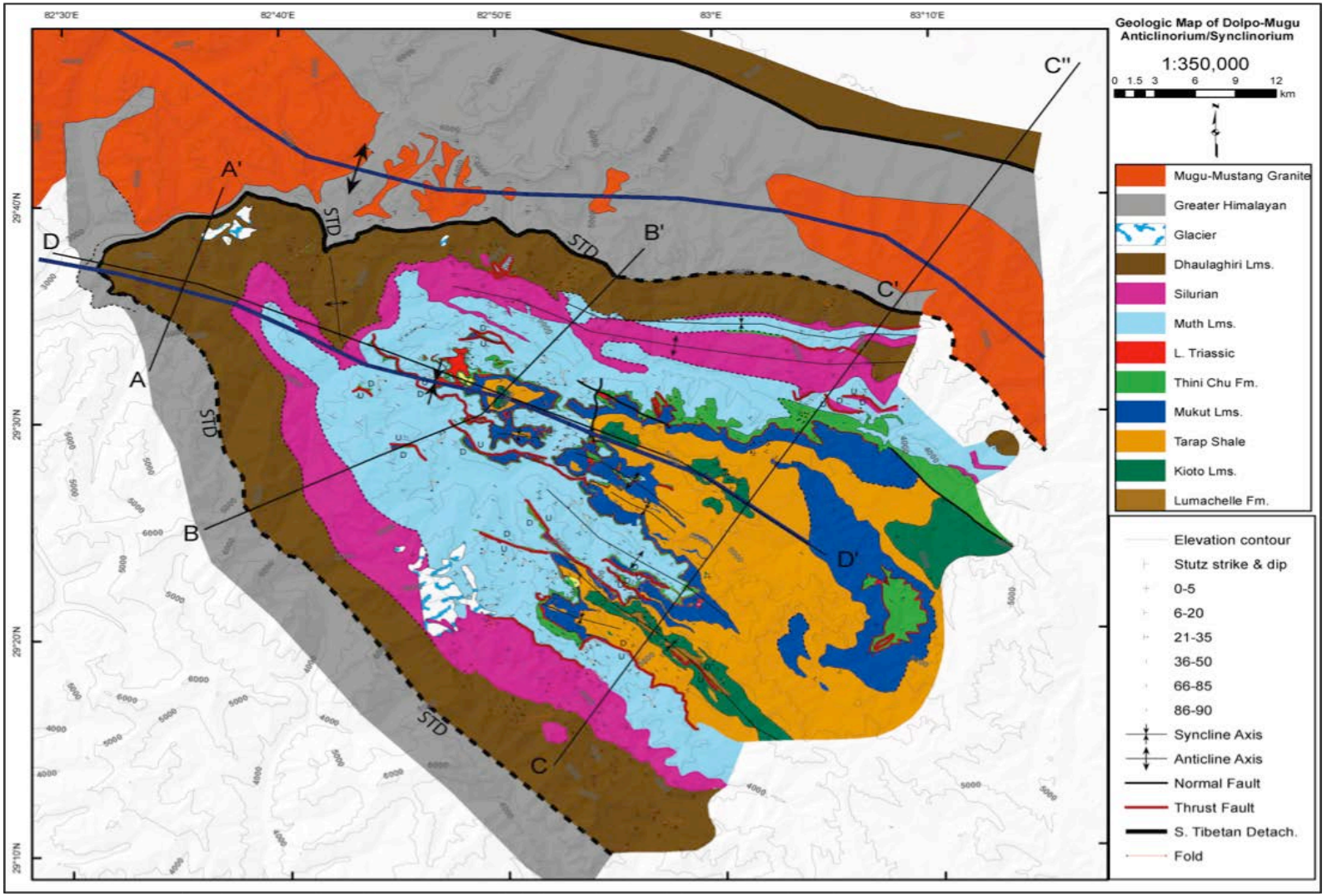

Figure 6. Geologic map of Dolpo-Mugu folds, adapted from Fuchs 1977.

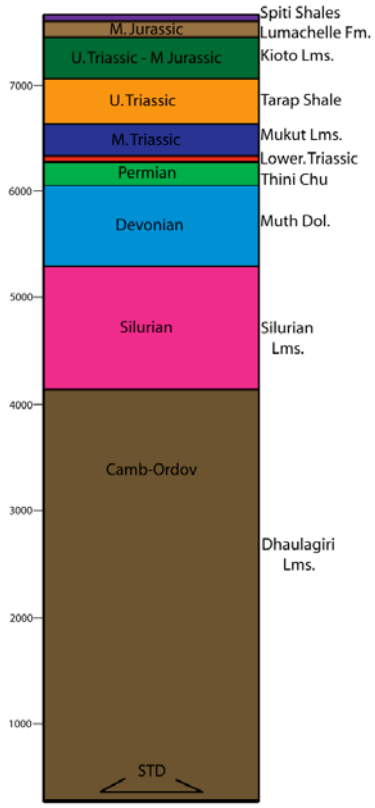

Figure 7. Generalized stratigraphic column of the Tethyan Himalayan Sequence in the Dolpo-Mugu synclinorium.

carbonate-biotite gneisses, and medium-grained biotite schists (Fuchs 1977).

The upper section of this thick carbonate sequence is the limestone portion of the Dhaulagiri formation. This consists of rhythmic alterations of fine-grained limestones, silty limestones, calcareous sandstone and siltstone, carbonate schists, and rare occurances of dolomite (Fuchs 1977). Sedimentary structures such as graded bedding, ripple cross-laminations, and current bedding suggest a dynamic depositional environment.

Silurian Limestones and Dolomite

The Silurian is represented as series of variable limestones and carbonate quartzites. There is significant variation from section to section of the Silurian, but commonly it is observed that the base and the top of the Silurian are composed of blue-grey marly limestones, silty limestones, and dolomite. The center sections of the Silurian are generally composed of multi-colored (red, green, grey, purple) schistose carbonates and rare dark slate. At any particular location any member may be missing from the sequence. For example, in the Phoksundo region the red and purple sediments disappear from the northwest to the southeast, and a band of green-grey and dark silty slates is present towards the southeast. The thickness of this formation is highly variable, ranging from 150-200 m in some locales to as much as 1000 m in other places (Fuchs 1977).

Muth Dolomite

The Devonian aged Muth dolomite varies in thickness from 800-1200 m. It is predominantly composed of thick-bedded, massive dolomites that are light grey to almost black in color. Banding, fine laminations, occasional graded bedding, oolites, intraformational breccias, ripple cross-laminations, ripple marks, and desiccation cracks are among the sedimentary structures that characterize the Muth dolomite and indicate a shallow marine depositional environment (Fuchs 1977).

Thini Chu

Fuchs dated the Thini Chu formation as Permian, but later researchers have suggested an age for the Thini Chu of mid-Carboniferous to Permian (Garzanti, 1999). The Thini Chu is composed of white, grey, and green quartzites and conglomerates, sandy limestones and silty or sandy shales. Current bedding and burrows suggest a deep shelf depositional environment (Fuchs 1977). In some areas the Thini Chu is only 30-70 m thick, whereas in other areas it is several hundred meters thick.

Scythian Limestone (L. Triassic)

The Scythian formation is a marker bed at the base of the Triassic. Deposited above the Thini Chu, the Scythian formation is composed of thin-bedded and dense limestones that are light grey, brown, and dark grey in color. Subordinate grey shales are occasionally found interbedded. The Scythian formation is weather resistant and can be identified from afar, being easily traceable in the field (Fuchs 1977).

Mukut Limestone

Stratigraphically above the Thini Chu formation is the middle Triassic Mukut formation. The Mukut limestone is an intensely folded layer varying from 50 to 300 meters in thickness. It is a well bedded dark blue limestone with dark marls and rare black shales (Fuchs 1977).

Tarap Shales

The Tarap formation of upper Triassic age is dark grey or green silty shale with impure sandstone stringers. The thickness varies between 300-400 m, but in places is tectonically reduced to tens of meters. The Tarap shales compose a significant portion of the outcropping TSS in the Dolpo synclinorium.

Quartzite beds and Kioto Limestone

Of very late Triassic to mid Jurassic age, the quartzite beds and Kioto limestones deposited after the Tarap shales have a cumulative thickness of 200-400 meters. The quartzite beds are about 50 m thick, and alternate between green/white/grey/brown quartzites, carbonate quartzites, sandy dolomites, blue/grey limestones, marls, and grey/green shales. The quartzite beds indicate a marked regression in the formation, and are noticed throughout the Himalayan Tethys (Fuchs 1977).

The Kioto limestone above the quartzite beds is a thick bedded, light-dark grey or blue limestone and dolomite package. A few arenaceous beds are occasionally interbedded.

Lumachelle limestones and shales

Representing the middle Jurassic is the Lumachelle formation. These thin bedded grey/dark blue limestones, marls, and dark shales appear only rarely in the Dolpo synclinorium. Fuchs (1977) reports that they appear only in the region south of Sya Gompa.

Spiti shales

The highest stratigraphic unit of the Tethyan Sedimentary Sequence in the Dolpo area is the upper Jurassic Spiti shale formation. Like the Lumachelles, this formation is rare in the Dolpo synclinorium and was observed only in the same region as the Lumachelle formation This attenuated, black shale contains concretions as well as fragments of belemnite.

3.2 Greater Himalayan Leucogranites

The Greater Himalayan rocks are intruded by discrete leucogranitic bodies found within all units of GHC rocks. These granites, which appear in scale ranging from sills and dikes a few centimeters across to plutons of several hundred kilometers, were produced from anatectic melting of GHC rocks, especially Formation 1 (Le Fort et al, 1987). The age, range, and relationships of these leucogranites have been very influential in models of Himalaya evolution (Hodges, 2000).

In the Dolpo-Mugu region the Mugu leucogranite intrudes the GHC. Based on their field relationships with respect to deformational fabrics, it appears that the Mugu leucogranites represent several distinct episodes of anatactic melting. This granite has been dated as ca. 20.76 Ma to ca. 17.6 Ma. (Hurtado et al., 2007).

The Mugu leucogranite is a light colored, fine to medium grained, two-mica granite with pegmatites containing garnet, silliminite, tourmaline, biotite, and muscovite (Fuchs, 1977). This description is similar to other leucogranites in the region such the Manaslu leucogranites just north of the Annapurna range. That granite intrusion is described as a sill located along the top of the GHC (Godin et al., 2006). The Manaslu leucogranites are thought to be a minimum-melt granite derived from a source similar to Formation I of the GHC. This leucogranite is dated to ca. 22.9 Ma to 19.3 Ma (Harrison et al., 1999).

4. STRUCTURAL GEOLOGY OF DOLPO-MUGU SYNCLINORIUM

Fuchs mapped the Dolpo-Mugu synclinorium in 1977 (Fuchs, 1977) and his mapping provides the framework for investigating folding and shortening across the fold (figure 6). The axial traces of these folds, inferred from mapping by Fuchs (1964; 1973), extend for ~200 km and have a half wavelength of between 20-50 km, and are south verging. The core of the synform contains Mesozoic sedimentary rocks that are part of the THS which has a minimum thickness of ~9 km (Fuchs, 1964; Colchen et al., 1981). The core of the antiform is composed of GHC rocks (LeFort, 1976). The structural relief between rocks exposed in crest of the antiform to the trough of the synform is >9 km. The wavelength and structural relief of these folds, and the observation that Greater Himalayan rocks are involved in the folding, indicates that deformation is deep-seated in the Himalayan orogenic wedge.

4.1 Identification of the South Tibetan Detachment

Early workers in the area did not detect the presence of the STD and interpreted there to be no tectonic disturbance at this boundary; it was thought that the Dhaluagiri limestone gradually passes through higher grades of metamorphism as it merges into the GHC crystallines below in one lithologic succession. (Fuchs 1977). However, later mapping has identified the presence of the STD along the strike of the Himalayan orogen serving as the boundary between the THS and GHC for a total of over 2000 km (Searle and Godin 2003) from Zanskar (Searle and Rex

1989; Searle et al. 1999; Walker et al. 1999) to South Tibet (Burchfiel and Royden 1985; Burchfiel et al. 1992).

Fuchs distinguished between the base of the Dhaulagiri limestone and metamorphic carbonates structurally beneath. That contact is interpreted as the location of the STD in this study. The metamorphic carbonates below the Dhaulagiri limestone are pervasively intruded by Mugu-Mustang leucogranites. This possibly correlates with the intruding Manaslu leucogranite north of the Annapurna range. Early workers described the Manaslu granite as intruding across the STD into the unmetamorphosed sediments of the Tethyan sedimentary sequence. However, p-t conditions of the carbonate rocks into which the Manaslu granite is intruded are high and do not show signs of contact metamorphism (Schneider & Masch 1993). Searle and Godin (2003) place the Manaslu leucogranites wholly within the GHC, similar to all other Himalayan leucogranites. Research continues into the structural relationships between the leucogranites and the STD, but present knowledge suggests that the Mugu-Mustang leucogranites are entirely below the STD in this region.

4.2 Folding within the Synclinorium

Strike and dip measurements from within the synclinorium come from two sources: Fuchs' approximate measurements and new strike and dip data retrieved remotely (below). Fuchs' dip measurements were published as ranges, (0-5°; 6-20°; 21-35°; 35-50°; 51-65°; 66-85°; 86-90°) , the exact strike angles were not published,

except as they are represented by the orientation of their symbol on Fuchs' geologic map. For the present study Fuch's strike measurements were individually measured on the geologic map (Appendix B).

A limited amount of other strike and dip data was determined remotely through the three-point-problem methodology using Google Earth satellite imagery. These were used primarily for reconstructing cross-section A-A'. An explanation of this methodology is given in Appendix A.

The geologic map of the Dolpo-Mugu synclinorium clearly shows the secondary folding within the synclinorium. The axis of the synclinorium itself, though it curves gently, strikes in a NW-SE direction. Its secondary folds generally strike parallel to the synclinorium axis, although in several places they strike obliquely to the synclinorium. One prominent exception to this rule is a large northward-plunging anticline along the Changdi Khola valley that strikes almost perpendicular to the synclinorium. Reverse faulting within the synclinorium also generally strikes NW-SW.

Stereonet projections (figure 8) illustrate the character of the synclinorium and some of its secondary folds. Folds strike NW-SE with a shallow, but consistent, plunge to the SE. The stereonet projections also illustrate a trend that is perhaps less obvious on the geologic map: observing fold axis orientations successively from north to south reveals that they incrementally pivot clockwise across the synclinorium. The axes of the folds along the northern limb of the synclinorium

trend S64°E, and successive trends become more southerly until fold axes in the southern limb of the synclinorium which trend S44°E.

4.3 Cross Sections and Shortening

Cross sections were constructed across the synclinorium: three perpendicular to the strike of the folds and one along-strike (figures 6, 9A, 10A, 11A, 12A). Each of these cross sections is accompanied by a second cross section that predicts the orientation of bedding and THS folds before the STD folded (figures 9B, 10B, 11B, 12B).

Shortening across these cross sections was calculated for three horizons: The STD, the top of the Dhaulagiri limestone, and the top of the Mukut limestone (Table 1). In each case "absolute shortening" and "percent shortening" can be predicted. Absolute shortening refers to total shortening across the cross section in kilometers. This can be calculated by measuring the lengths of formation contacts including the portions which are folded, and contrasting that with an absolute length which measures a straight line across the cross section. For this study absolute shortening estimates were calculated using measurements along the STD, along the top of the Dhaulagiri limestone, and along the top of the Mukut formation. Among the across-strike cross sections that were constructed, cross section A-A' predicts ~3 km of shortening (average 3.005 km), cross section B-B' predicts ~6-7 km of shortening (average 6.66 km), and cross section C-C' predicts 3-7 km of shortening (average 5.37 km). See Table 1 for details.

Percent shortening represents the percentage of original crustal length that is lost due to uplift and folding. Percent shortening perpendicular to strike is most pronounced towards the nose of the plunging synclinorium (cross section A-A'), and decreases towards the south-east as the synclinorium opens up. Cross section A-A' predicts 20-28% shortening (average 24%), cross section B-B' predicts 16-19% shortening (17.33%), and cross section C-C' predicts 6-14% shortening (average 11%). See Table 1 for details.

4.4 The Effect of STD Folding on the orientation of THS folds

As discussed above, STD activation and folding post-dates the smaller scale folding of THS formations. In order to evaluate the effect of STD regional folding on the orientations of these older THS folds it was necessary to "unfold" the THS by constructing cross sections that illustrate the orientations of THS formations and their folds before the STD was folded (figures 9B, 10B, 11B, 12B). In each case the STD is restored to an unfolded orientation, and strike and dip measurements are taken along the limbs of various smaller scale THS synclines, and then contrasted with the orientation of those same limbs after STD folding as depicted in figures 9A, 10A, 11A and 12A. The resulting rotations of the limbs of these synclines are illustrated in figures 14A and 14B, and their exact strikes, dips, and axial plane orientations are recorded in appendix C.1 and C.2.

In cross section A-A' the orientations of two synclines were measured both before and after they were rotated by folding of the underlying STD (for the

locations of the synclines see figures 9A and 9B). The stereonet plots of these limbs are illustrated in figure 14A. Syncline 1 of cross section A-A' is on the SW limb of the regional STD fold, and syncline 2 is on the NE limb. Each of these synclines was accordingly rotated by the STD, with their respective axial planes being rotated toward the axis of the STD regional fold.

The folds in cross section A-A', unlike folds in other cross sections, were also rotated by the plunging nature of the regional synclinorium which is focused in the nose of the synclinorium. The plunging nature of the STD in this location is best illustrated in cross section D-D' (figure 12A). As will be illustrated by structure maps below, the plunging STD in the nose of thy synclinorium plunges from 43º to 23º on average. The structurally higher THS formations plunge at lower angles, with a THS syncline in cross section D-D' rotated approximately 12º. (see figure 14B, appendix C.2 and figure 12B. D-D' strikes perpendicular to the axis of the synclinorium, and the THS small-scale syncline measured along D-D' strikes parallel to the axis of the STD plunge). Therefore, it is surmised that the axial planes in synclines in A-A' are not only rotated towards the axis of the synclinorium, but also gain a plunge of 12º in a SE direction.

The orientations of synclines in cross sections B-B' and C-C' were also analyzed. Figures 14A and 14B illustrate that the amount of rotation these limbs underwent as a result of STD folding was a function their position along the STD fold. Those folds structurally above steeper STD folding were rotated more, while

those folds closer the center of the synclinorium, where STD folding is less pronounced, were rotated less.

A fold can be described on the basis of the orientation of its axial plane. Following the system of Davis and Reynolds, 1996, the orientations of axial planes of each measured syncline is illustrated in figure 13 (precise data is provided in Appendix C.2). The synclines, pre-STD folding, were generally “upright to steeply inclined with horizontal plunges”. However, after STD folding several locations were rotated to such a degree that they now are “upright to steeply inclined with gently dipping plunges”. These locations are focused in the nose of the synclinorium, in cross section A-A’.

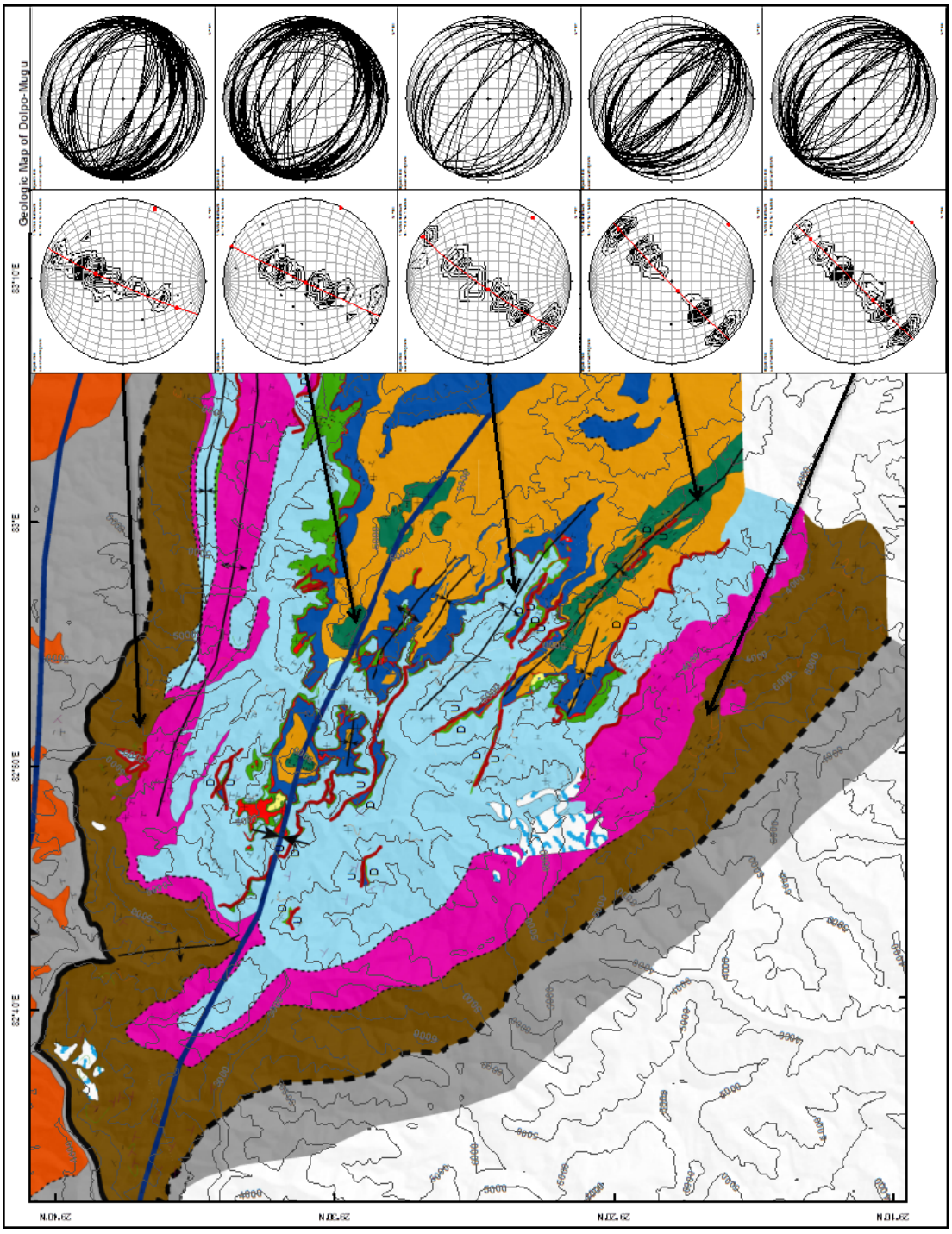

Fig. 8 Stereonet plots for the synclinorium limbs and selected THS folds.

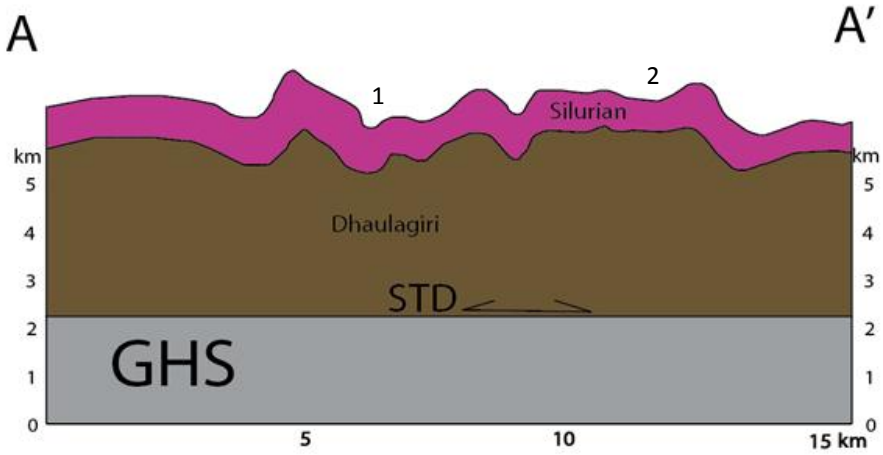

Figure 9A: Cross section A-A'. Numbers 1-2 in the image are synclines whose orientations were analyzed pre- and post-STD folding.

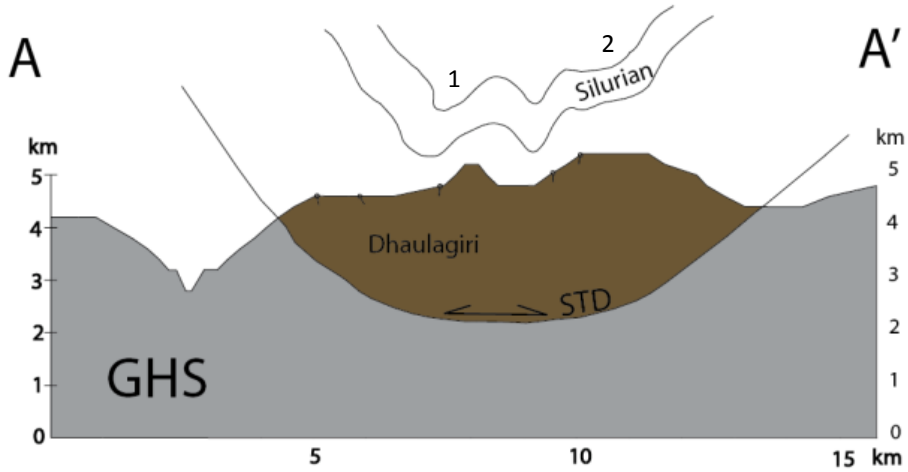

Figure 9B: Cross section A-A' restored to pre-STD folding time. Numbers 1-2 in the image are synclines whose orientations were analyzed pre- and post-STD folding.

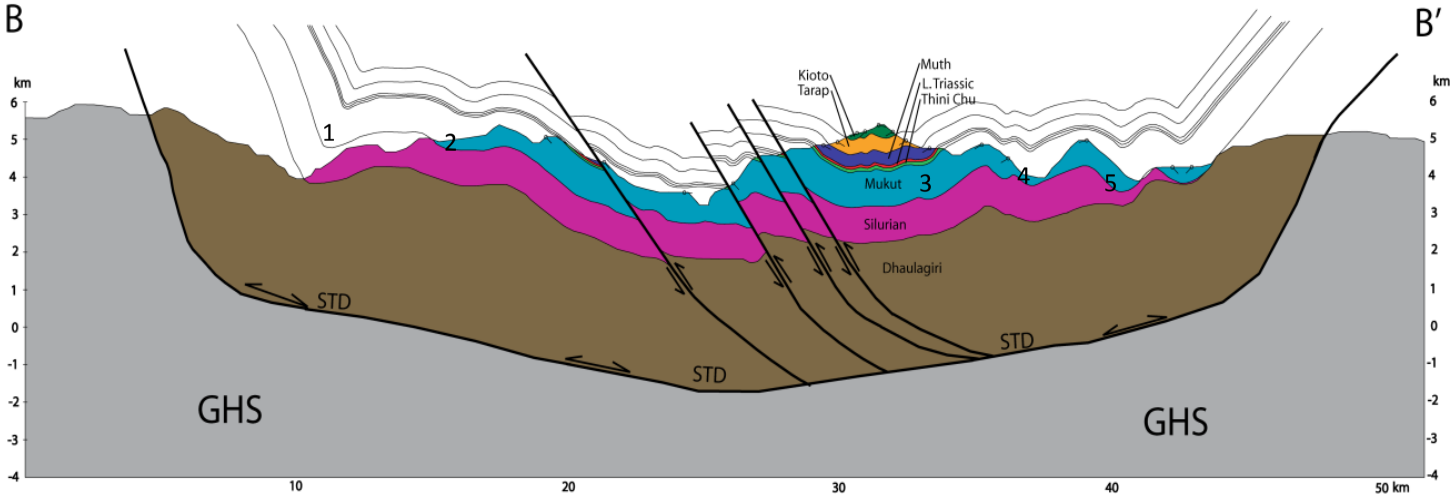

Figure 10A: Cross section B-B'. Numbers 1-5 in the image are synclines whose orientations were analyzed pre- and post-STD folding.

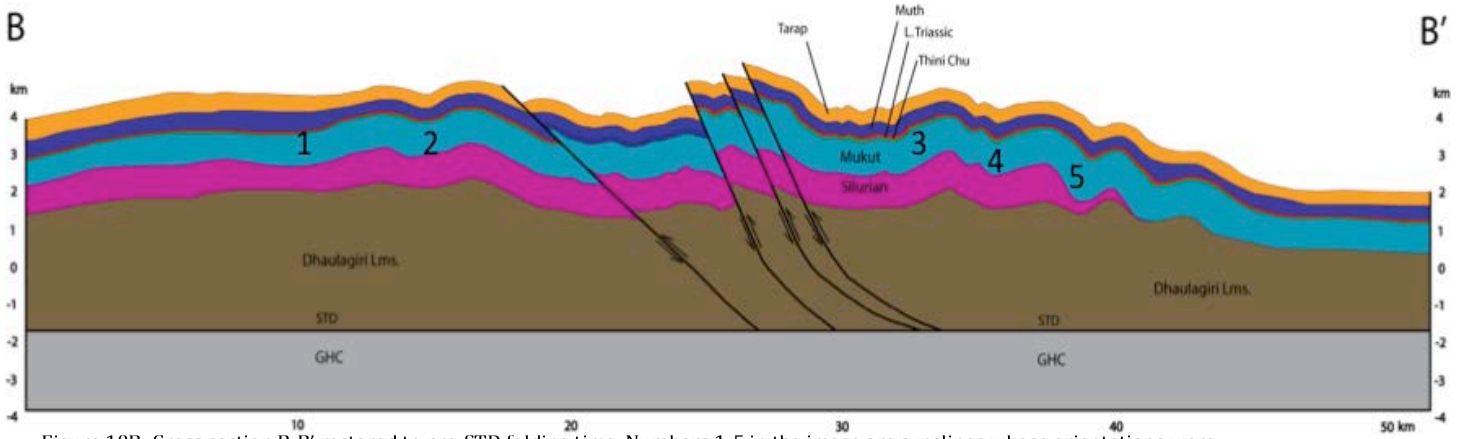

Figure 10B: Cross section B-B' restored to pre-STD folding time. Numbers 1-5 in the image are synclines whose orientations were analyzed pre- and post-STD folding.

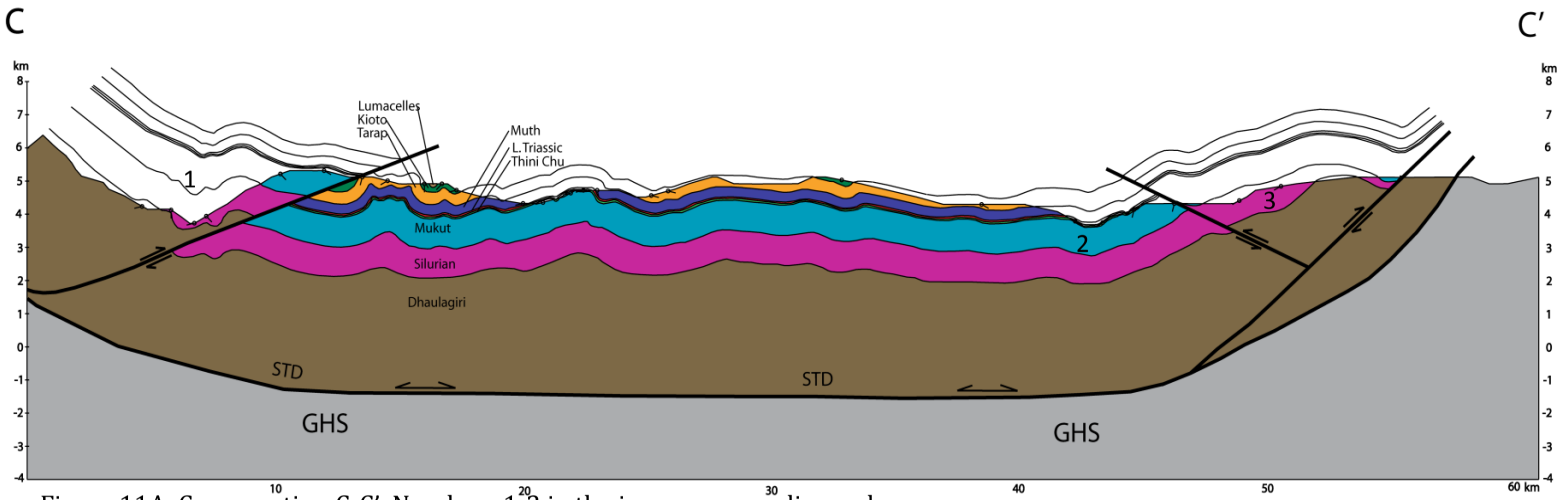

Figure 11A: Cross section C-C'. Numbers 1-3 in the image are synclines whose orientations were analyzed pre- and post-STD folding.

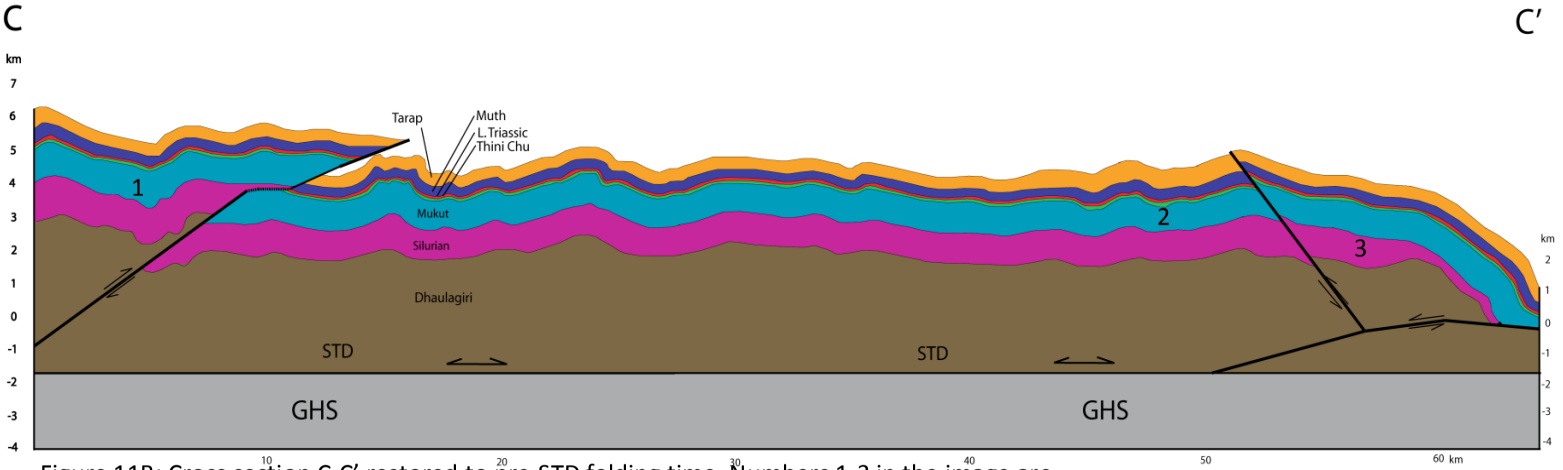

Figure 11B: Cross section C-C' restored to pre-STD folding time. Numbers 1-3 in the image are synclines whose orientations were analyzed pre- and post-STD folding.

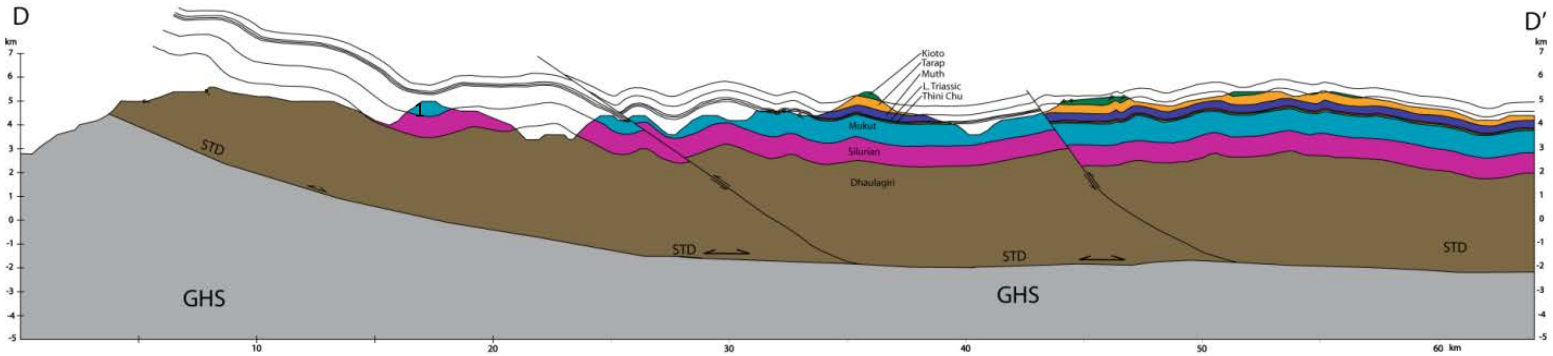

Figure 12A: Cross section C-C'. Numbers 1-3 in the image are synclines whose orientations were analyzed pre- and post-STD folding.

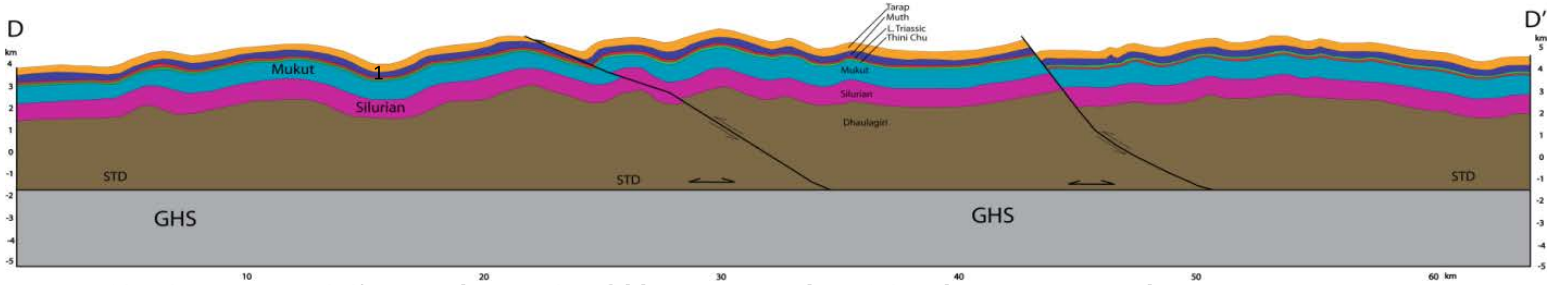

Figure 12B: Cross section C-C' restored to pre-STD folding time. Numbers 1-3 in the image are synclines whose orientations were analyzed pre- and post-STD folding.

A	STD	Dhaulagiri
A : Absolute Shortening	3.14 km	2.87 km
A: Percent Shortening	20%	28 %

B	STD	Dhaulagiri	Mukut
B : Absolute Shortening	7.28 km	7.16 km	5.54 km
B: Percent Shortening	16 %	19 %	17 %

C	STD	Dhaulagiri	Mukut
C : Absolute Shortening	2.98 km	7.00 km	6.13 km
C: Percent Shortening	6%	14%	13%

Table 1. Absolute and relative shortening across three cross sections: A-A', B-B', C-C'.

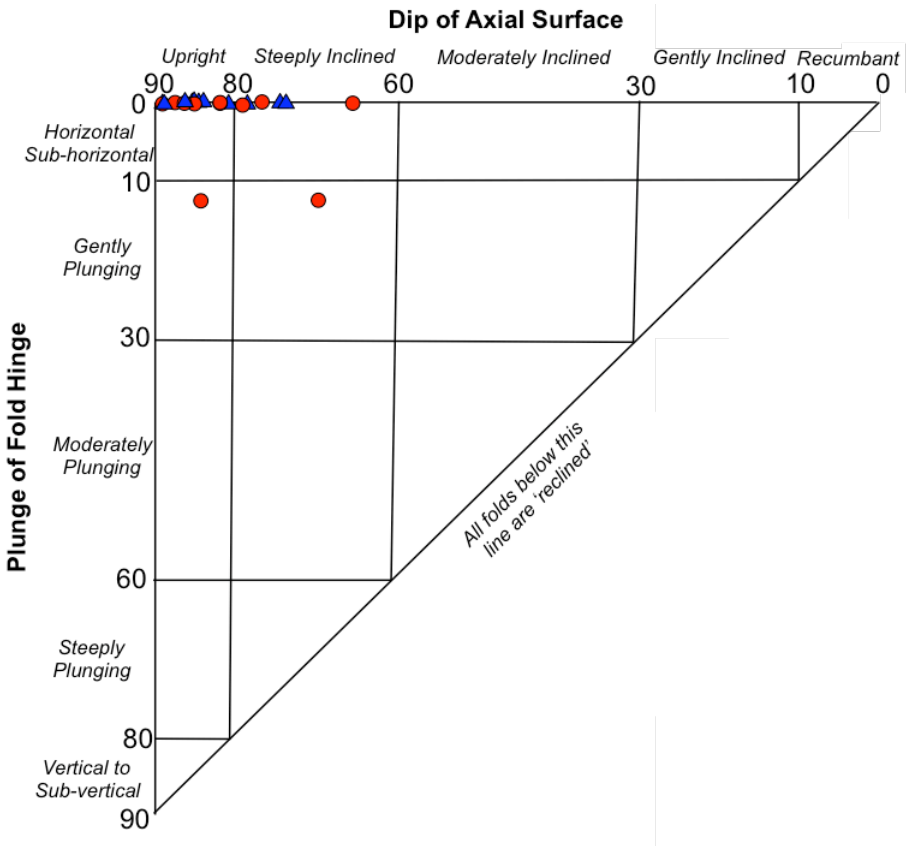

Figure 13. The orientations of eleven syncline axial planes in THS formations are represented above (modified from Davis and Reynolds, 1996). Blue triangles represent orientations pre-STD folding, and red circles represent orientations of the same axial planes post-STD folding.

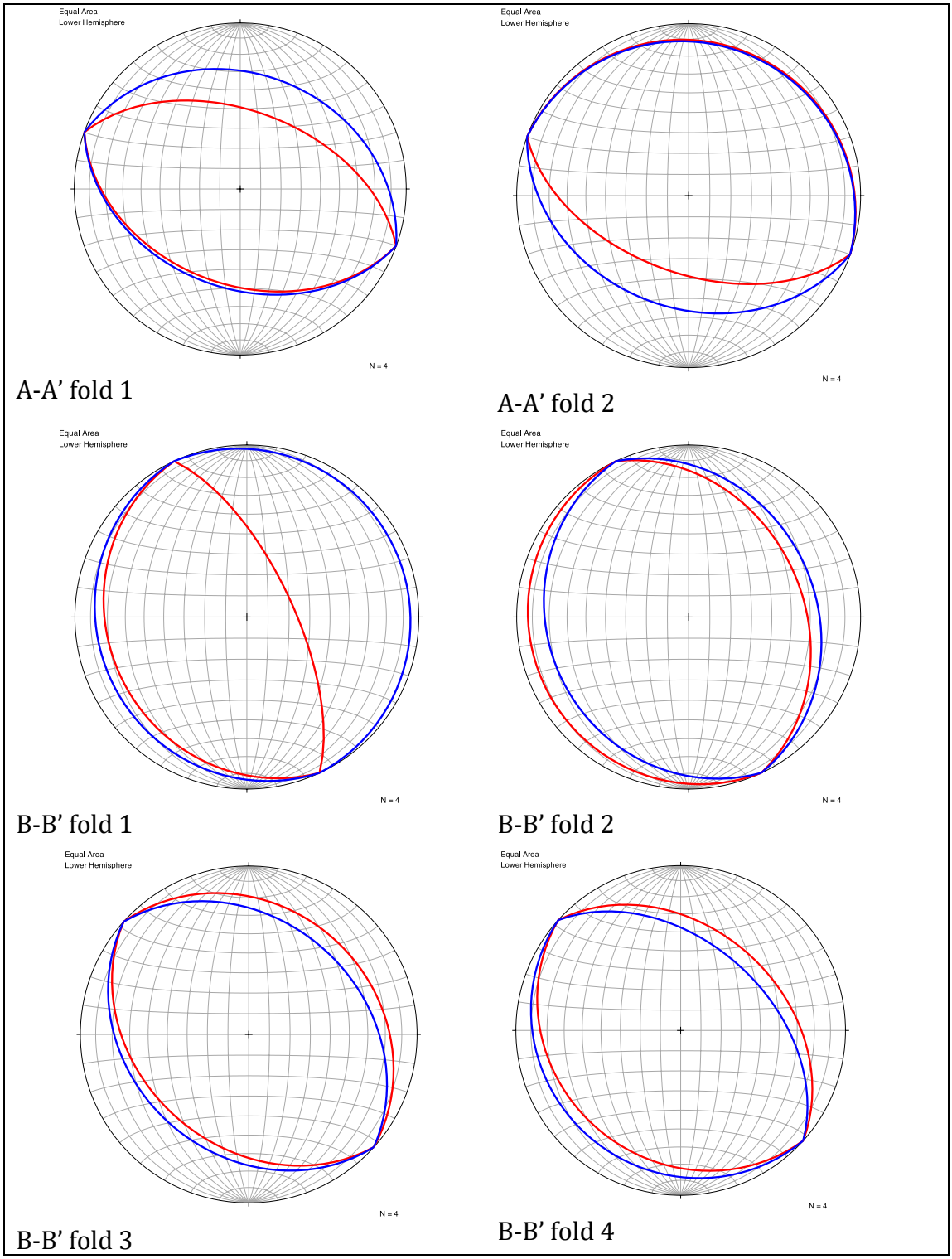

Figure 14A. A-A' folds 1 and 2; B-B' folds 1, 2, 3 and 4. Blue represents orientations of folds before STD folding, red represents orientations of folds post-STD folding.

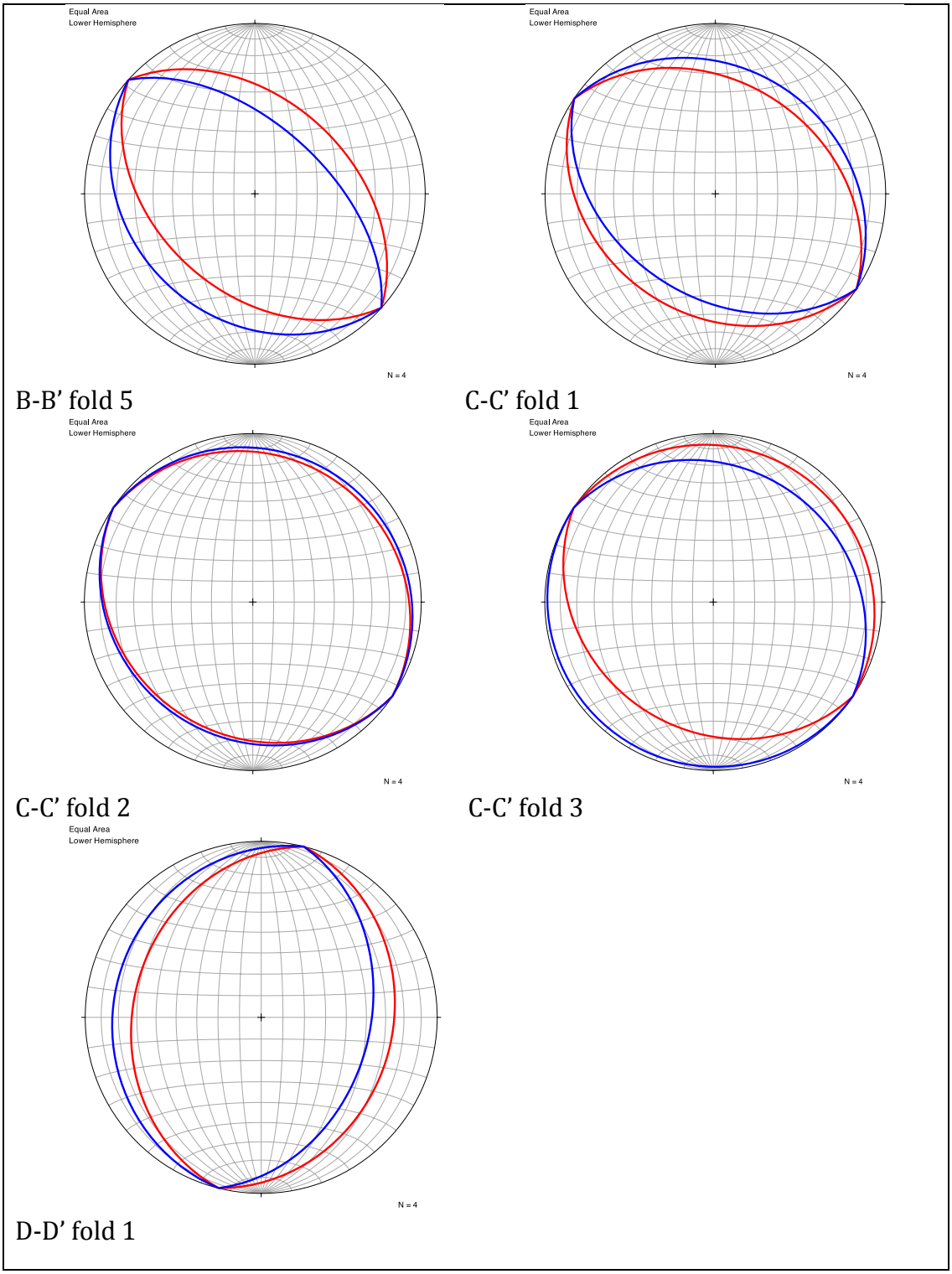

Figure 14B. B-B' fold 5; C-C' folds 1, 2, and 3. Blue represents orientations of folds pre- STD folding, red represents orientations of folds post-STD folding

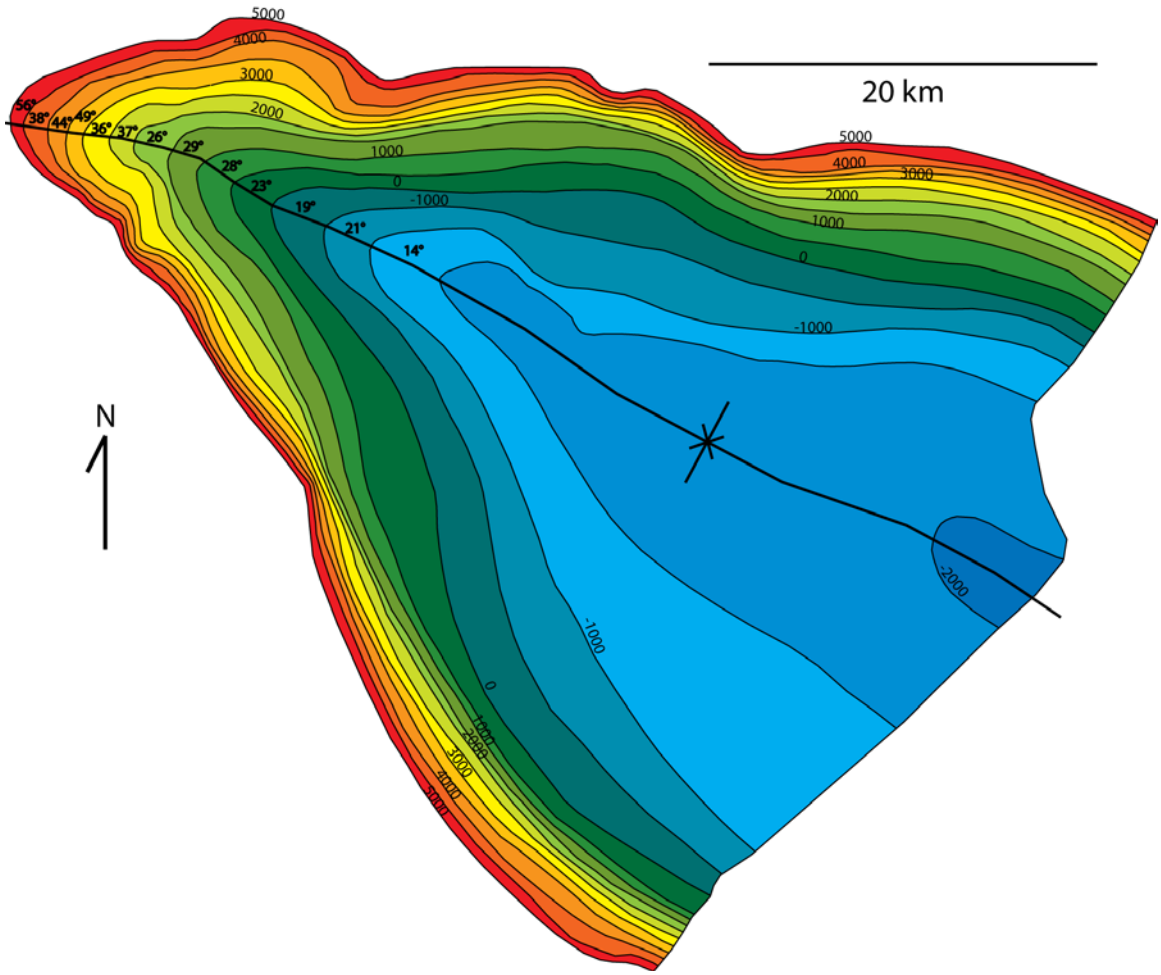

Figure 15A. Structure contour map of STD within the Dolpo-Mugu synclinorium. Contours are in units above sea level, with a contour interval of 500 m.

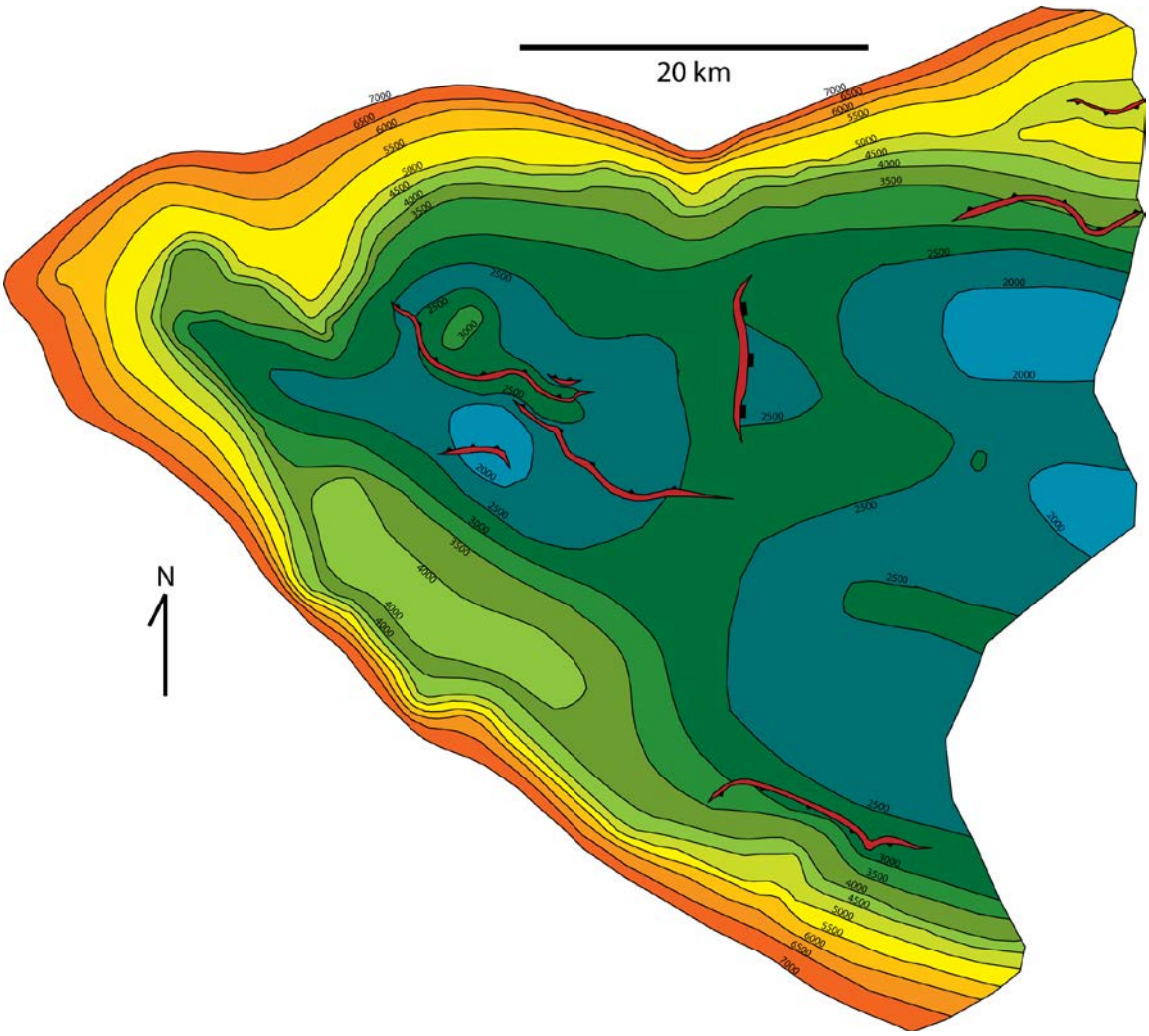

Figure 15B. Structure contour map of Dhaulagiri within the Dolpo-Mugu synclinorium. Contours are in units above sea level, with a contour interval of 500 m. Faults are represented in red.

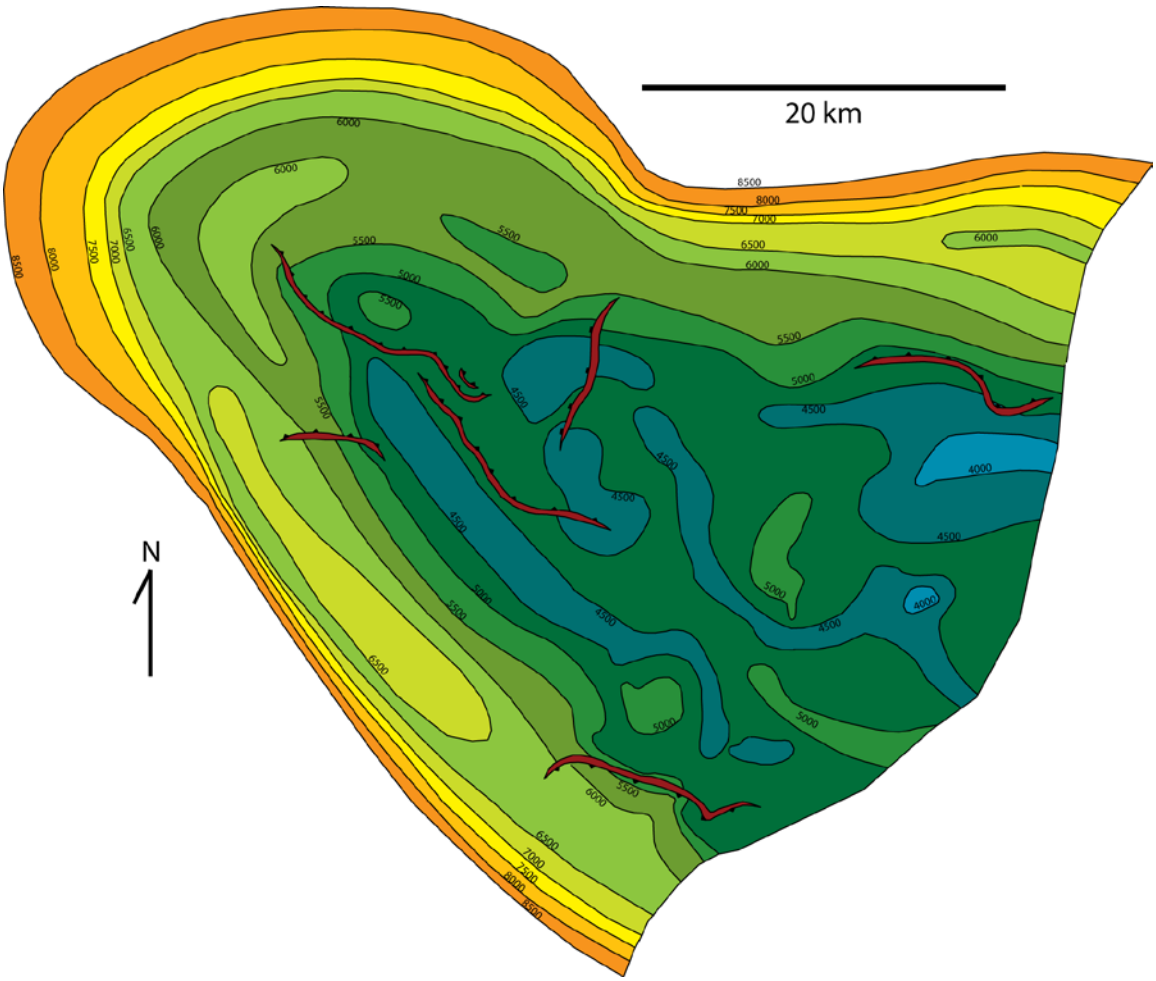

Figure 15C. Structure contour map of Dhaulagiri within the Dolpo-Mugu synclinorium. Contours are in units above sea level, with a contour interval of 500 m.. Faults are represented in red.

4.5 Structural Character of the Synclinorium

The southeasterly plunging synclinorium, as observed in the cross sections, has steep dip along its limbs and becomes shallower toward the axial plane at every stratigraphic level. This becomes increasingly clear when illustrated by structure contour maps (figure 15A, 15B, 15C).

Structure contour maps of the STD, Dhaulagiri limestone, and Mukut limestone were hand drawn using depth information from the series of cross sections in figures 9A, 10A, 11A, and 12A and elevation contours at outcrops on the geologic map (figure 6). The STD, being the lower boundary of the THS, does not have the small-scale folding that developed in the THS prior to STD slippage and folding. All horizons have their steepest dips at points furthest from the axis of the synclinorium.

Figure 15A illustrates variations in plunge along the axis of the folded STD. The steepest plunge is in the nose of the synclinorium where it averages 43° and then shallows to an average of 21°, and then finally becomes very shallow moving away from the nose toward the SE. Bedding dip along the limbs of the synclinorium average 27-38° in the northern limb and 38-42° in the southern limb; the southern limb generally has slightly steeper dip than the northern limb, causing the synclinorium to verge NE.

5. DISCUSSION

5.1 Possible Fault Architecture below the Synclinorium and Predicted Shortening and Crustal Thickening

Three primary hypotheses for fault geometry are possible that relate to fold development. These are (A) a duplex, (B) a fault-bend-fold, or (C) a blind thrust. Figures16A, 16B, and 16C show these three possible variations of cross section C-C'' (figure 6) which extends to the NE in order to predict the sub-surface of the anticlinorium. For purposes of simplicity the Mugu-Mustang leucogranites present within the GHC are not illustrated in these cross-sections, and are considered together with the GHC as one unit. Crustal thickening of the anticlinorium in each of the models suggested here is estimated to be 10-11 km of vertical thickening, or ~45% increase in GHC crustal thickness. In each model "absolute shortening" and "percent shortening" across the entire length of C-C", which spans both the synclinorium and the anticlinorium, can be calculated (Table 2).

	Absolute Shortening	Relative Shortening
Duplex	33.03 km	30%
Fault-bend fold	25.13 km	24%
Blind thrust	8.2 km	10%

Table 2. Absolute shortening and relative shortening predicted by each of the three hypotheses for fault architecture. Absolute shortening refers to net shortening in the GHC across cross section C and its extension through the anticlinorium. Relative shortening represents the percentage of original crustal length that is lost due to uplift and folding.

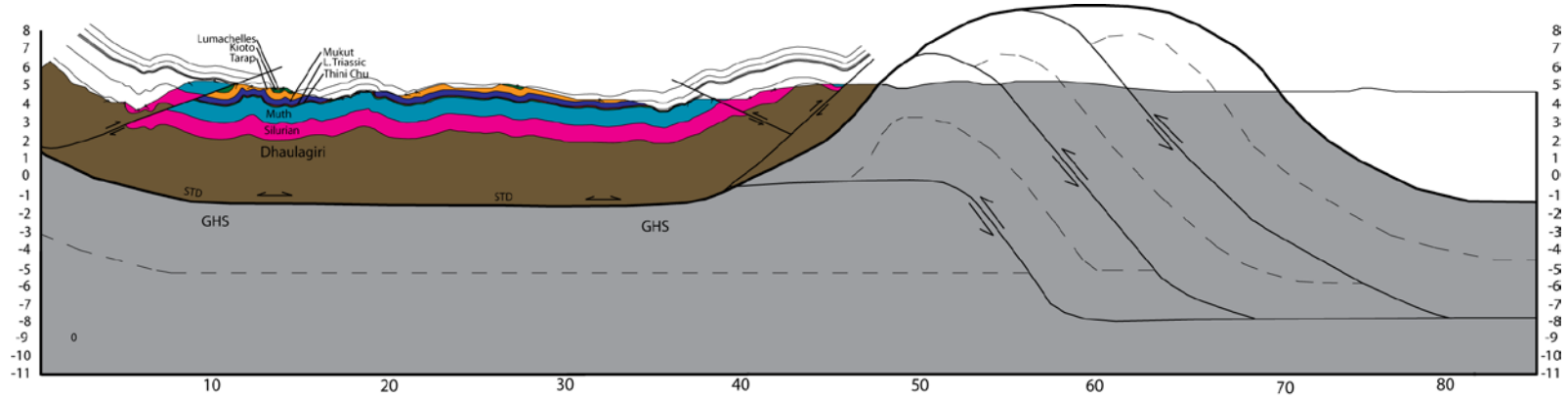

Figure 16A. Duplex model

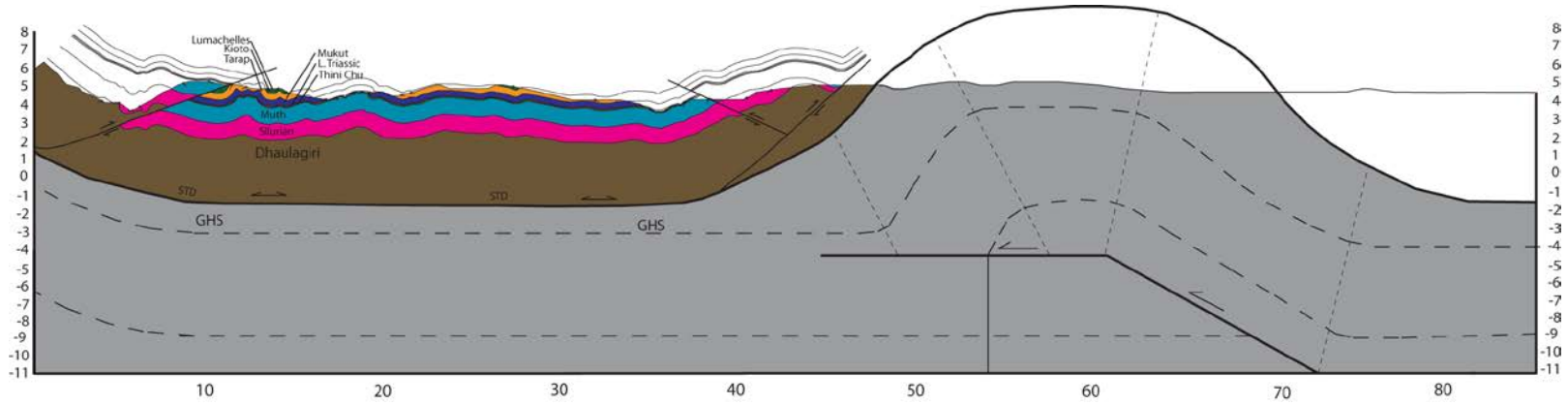

Figure 16B. Fault-bend fold model.

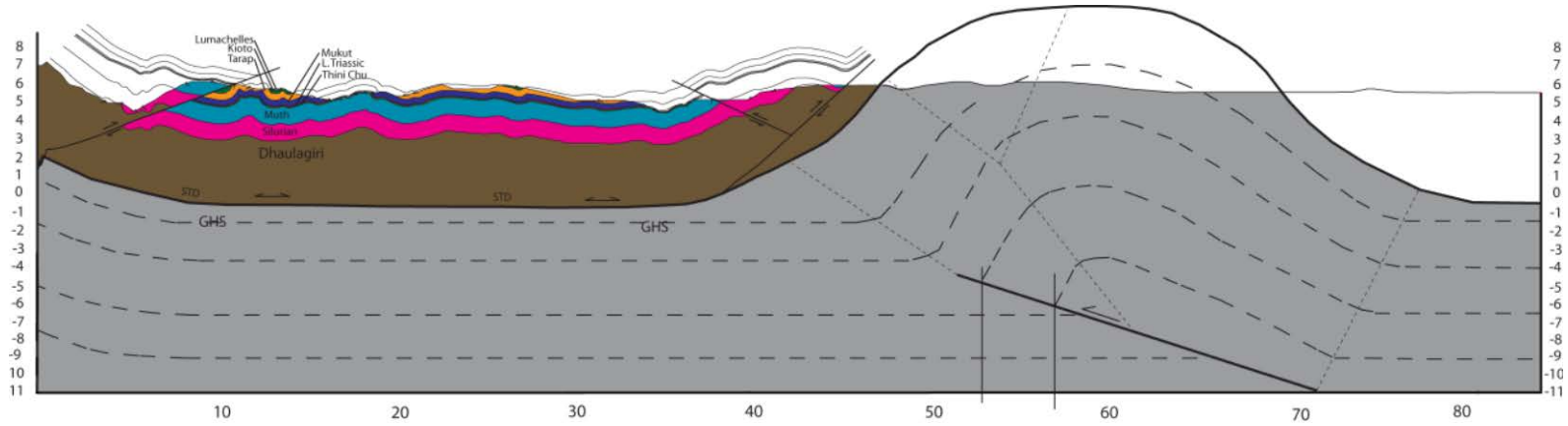

Figure 16C. Blind thrust model

Duplex

If development of a duplex is responsible for the anticlinorium it would represent the maximum amount of shortening possible. Figure 16A suggests the possibility of three to four large horses defined by subsidiary faults at 15-20° root into an intra-GHC floor thrust, and have their termination in the STD above which is the roof thrust for the structure. This model predicts ~33 km of shortening with 30% relative shortening of original crustal length. However, it is possible that a greater number of horses with more complex geometries exist which could predict even greater shortening. The model proposed here predicts that slip along the STD during development of the duplex is localized to the portion of the STD spanning the horses, and no slip forward or hinterward of the duplex is necessary. In other words, the duplex could have developed within the GHC in the absence of bulk propagation of the GHC wedge.

Fault-bend fold

The development of the Dolpo-Mugu synclinorium and anticlinorium may be products of southward movement of GHC-THS thrust sheet over a crustal-scale ramp (figure 16B). This model predicts the anticlinorium and synclinorium developed as fault-bend folds. This geometry predicts the second greatest amount of shortening, with approximately 24% shortening across the anticlinorium/synclinorium for a total of ~25 km shortening.

Blind thrust

The third hypothesis for fault architecture is a blind thrust (figure 16C). A blind thrust rooted in the MBT or some intra-GHC detachment would terminate before reaching the STD. This would predict approximately 10% shortening across the anticlinorium/synclinorium for a total of ~8 km of shortening.

5.2 Regional Extent of Dolpo-Mugu Folds

The Dolpo-Mugu folds may be related to similar large scale folds to the east and west of the Dolpo-Mugu folds. In the Manaslu region of central Nepal, east of the Thakkhola graben and approximately 200 km from the Dolpo-Mugu folds, there is a pair of large-scale folds called the Chako antiform and Mutsog synform. Like the Dolpo-Mugu folds these folds developed after slip on the STD ceased and have GHC in the core of the antiform and THS in the core of the synform. The hinge of the Mustog synform plunges 10° towards the NW. The Chako antiform plunges 8° to the NW. The folds are upright, open folds with amplitude of ~4 km and a wavelength of ~25 km (Gleeson and Godin, 2006). The large magnitude of these folds, like the Dolpo-Mugu folds, implies crustal-scale folding.

West of the Dolpo-Mugu region is the Gurla Mandhata metamorphic core complex. This complex is ~100 km long in the east-west direction (parallel to strike) and ~40 km in the north-south direction. Murphy (2007) identified Lesser Himalayan sedimentary rocks in this region which, as noted earlier, is a lithotectonic

unit structurally beneath than the THS and GHC. The complex sits atop a large antiform that has a corresponding southern synform. Unlike the models presented for the Dolpo-Mugu folds which place shortening structures entirely within the GHC, fault architecture within the Gurla Mandhata antiform have been interpreted to be a duplex structure or thrust fault within the LHS, which is at the core of the antiform, with horizontal shortening predicted to be a minimum of 100-150 km (Murphy, 2007). The fold pair has an approximate half-wavelength of 40 km and an approximate amplitude of 18 km.

	Gurla Mandhata	Dolpo-Mugu	Chako/Mutsog
Amplitude	~18 km	~ 10 km	~ 4 km
Half-wavelength	~ 40 km	~ 37 km	~ 25 km

Table 3. Amplitude and half-wavelengths of three folds in the region of central, central-west, and far northwest Nepal.

Assuming that the Gurla Mandhata core complex, the Dolpo-Mugu folds, and the Manaslu folds are related by a single deformational event or related events, the along strike extension of this folded section of the Himalayan orogen is ~350 km, which is a significant portion of its' total ~2000 km strike. However, this folded section may be linked to even larger scale features. Larson et al., 2010 show that the leucogranites of the Dolpo-Mugu region lie within the axial trace of the gneiss domes of the Greater Himalayan Antiform. This interpretation suggests that structural deformation in the Dolpo-Mugu area may be related to first order folding within the hinterland of the Himalaya that extends for ~700 km.

5.3 Implications for Tectonic Wedge Geometry

Previous tectonic wedge models of GHC extrusion show the GHC wedge as having uniform thickness throughout the central-west region of Nepal (Webb et al., 2007). The interpretation suggested in this study differs from previous interpretations by describing crustal shortening and vertical thickening within the GHC wedge in the Dolpo-Mugu region. As described above the tectonic wedge model predicts that STD and MCT branch from a single fault zone at the southern tip of the GHC wedge. This branch line is at least as far south as the southern edge of the Jarjarkot and Dadeldhura klippen as observed in regional geologic maps (figure 2).

5.4 Conclusion

Shortening from the Dolpo-Mugu folds ranges from 8-33 km, which does not appear to be sufficient to make up for the deficit in shortening budgets across the Himalayan orogen. The crustal thickening present in the Dolpo-Mugu folds is likely related to thickening in adjacent regions along strike. Detailed mapping and more precise strike and dip measurements along with focused field observations will help improve understanding of the Dolpo-Mugu synclinorium and anticlinorium and shed more light on sub-surface fault architecture responsible for crustal thickening.

6. APPENDICES

Appendix A: Google Earth and the Three-Point-Problem

Google Earth is quickly becoming the tool of choice for those interested in quickly and easily observing the Earth. Google Earth is a virtual three dimensional globe with a simple user interface that incorporates digitial elevation models and satellite imagery to bring suprisingly clear and accurate renderings of Earth's surface. These specifications will be explored further.

In the absence of on-location field data in hard-to-reach areas, Google Earth provides a means of measuring the strike and dip of stratigraphic units by employing the three-point-problem methodology. This computation can be accomplished if the following information is known: (a) elevation of three points within the plane to be measured, (b) latitude and longitude of the three points, (c) the distance and bearing from the highest of the three points to the second highest of the three points, and (d) the distance and bearing from the highest of the three points to the lowest of the three points. This data defines two vectors within the strike and dip plane which, when multiplied, yield a cross-product that represents the pole to that plane. The pole is then converted into familiar strike and dip coordinates. For this research data was calculated using a spreadsheet created by David T. Allison at the University of South Alabama. Throughout the area mapped by Fuchs (1973) the strikes and dips of exposed beds were calculated via the three-point-problem at forty-one locations. The locations of these stations and their strike and dip calculations can be found in Appendix B.

The three-point-problem methodology relies on an accurate digital elevation model and accurate geospatial positioning of satellite data. Using Google Earth for this task might be met with some resistance by those unfamiliar with the technical details of Google Earth's data. A brief discussion of Google Earth's data sources is appropriate. Google receives satellite images from a variety of sources, but this research project utilized images from only the GeoEye-1 satellite and the Quickbird satellite.

GeoEye

In 2008 Google became the exclusive online mapping site of imagery captured by GeoEye, Inc. GeoEye is a leading satellite imaging company with a number of satellites in operation. In 2008 GeoEye launched a satellite called GeoEye-1 that included the Google logo on the rocket. GeoEye-1 captures images from panchromatic cameras (at 0.41 m resolution) and multispectral cameras (at 1.65 m resolution), although only panchromatic images were utilized in this research. Due to government restrictions, GeoEye-1 provides Google with re-sampled panchromatic geospatial imagery at 0.5 m ground resolution instead if its maximum 0.41 m resolution. Half-meter ground resolution is currently the highest resolution commercially available. These images have much higher resolution than ASTER images (at 15, 30, and 90 m resolution) and LANDSAT images (at 15-30 m resolution).

Weighing in at 1955 kg (4310 lbs), GeoEye-1 also has an impressive geolocation accuracy. It boasts the ability to map features to within 5 meters of their actual locations without ground control points. The satellite makes fifteen orbits per day flying at an altitude of 681 km with an orbital velocity of about 7.5 km/sec. GeoEye-1 travels in a sun-synchronous orbit allowing it to pass over a given area at around 10:30 am local time every day. It has an inclination of 98 degrees from the equator and an orbital period of 98 minutes. Its nominal swath width is 15.2 km, and 9.44 km at nadir. Further technical details of the GeoEye-1 satellite can be found in the appendix.

Quickbird

The Quickbird satellite is owned and operated by DigitialGlobe, Inc. Quickbird was launched in 2001 from Vandenberg Air Force Base in California. Its panchromatic images are at a resolution of 0.65 m, and multispectral images are capable of 2.62 m resolution. Only the panchromatic images were utilized in this research. Again, this is higher resolution than both ASTER and LANDSAT images. At 952 kg (2100 lbs), Quickbird locates features to within 23 m of their actual locations without the use of ground control points. Quickbird orbits the Earth in a sun-synchronous fashion, with an orbital period of 94.2 minutes. Quickbird has a swath width of 18 km. Further technical details of this satellite can be found in the appendix.

Digital Elevation Model

Google Earth does not release technical details about the digital elevation models it employs. However, owing to the fact that NASA SRTM is freely available, it is assumed that in the Nepal region the DEM had an accuracy of at least 90 m. Extensive use if Google Earth in tandem with NASA SRTM in a GIS application (ArcGIS) indicates that Google Earth is in fact using SRTM, as no major discrepancies have been detected.

Appendix B.1

Fuch's Strike and Dip Measurements

Station	Latitude	Longitude	BedStrike	DipDirection	DipAngle	Avg Dip Angle
1	29.601467	82.544142	310.02	40.00	6_20	13
2	29.615089	82.542256	357.65	87.65	6_20	13
3	29.630469	82.562167	63.26	153.26	6_20	13
4	29.618069	82.569189	102.12	192.12	51-65	58
5	29.625864	82.572261	105.01	195.01	36-50	43
6	29.642622	82.568367	56.26	146.26	21-35	28
7	29.642214	82.582628	308.35	38.35	6_20	13
8	29.641839	82.597978	306.13	36.13	36-50	43
9	29.632653	82.603353	117.64	207.64	51-65	58
10	29.651056	82.611347	72.41	162.41	21-35	28
11	29.638153	82.621636	109.98	199.98	51-65	58
12	29.644392	82.626983	299.19	29.19	36-50	43
13	29.652781	82.629675	116.82	206.82	66-85	76
14	29.656717	82.635775	112.07	202.07	36-50	43
15	29.673294	82.643458	69.80	159.80	21-35	28
16	29.663822	82.644878	90.72	180.72	21-35	28
17	29.649183	82.656447	112.34	202.34	36-50	43
18	29.614122	82.669644	116.98	206.98	21-35	28
19	29.632472	82.673094	299.70	29.70	21-35	28
20	29.640975	82.675728	116.14	206.14	36-50	43
21	29.589431	82.685617	122.46	212.46	21-35	28
22	29.606817	82.703050	33.94	123.94	6_20	13
23	29.632933	82.709569	39.94	129.94	6_20	13
24	29.608231	82.713592	90.00		0-5	2
25	29.599692	82.723281	291.28	21.28	6_20	13
26	29.603494	82.724508	292.88	22.88	36-50	43
27	29.626522	82.729886	285.85	15.85	6_20	13
28	29.638914	82.758792	90.00	180.00	6_20	13
29	29.644664	82.779525	98.30	188.30	21-35	28
30	29.630344	82.796900	104.21	194.21	36-50	43
31	29.633389	82.796886	110.16	200.16	66-85	76
32	29.636475	82.798239	101.66	191.66	51-65	58
33	29.623067	82.805581	102.20	192.20	6_20	13
34	29.645417	82.816503	87.90	177.90	21-35	28
35	29.640028	82.817772	113.33	203.33	51-65	58
36	29.631403	82.820075	108.12	198.12	36-50	43
37	29.617014	82.820433	300.64	30.64	6_20	13
38	29.627639	82.824722	125.74	215.74	66-85	76
39	29.632972	82.827483	134.07	224.07	36-50	43

Appendix B.1 Continued

Station	Latitude	Longitude	BedStrike	DipDirection	DipAngle	Avg Dip Angle
41	29.650150	82.832439	109.41	199.41	36-50	43
42	29.616989	82.830883	309.17	39.17	6_20	13
43	29.633325	82.832067	332.44	62.44	36-50	43
44	29.635433	82.835111	139.59	229.59	51-65	58
45	29.632483	82.841206	141.12	231.12	51-65	58
46	29.617056	82.839011	14.97	104.97	6_20	13
47	29.618022	82.842444	287.63	17.63	66-85	76
48	29.628247	82.854039	124.33	214.33	36-50	43
49	29.626467	82.857422	90.00		0-5	2
50	29.602228	82.879378	289.89	19.89	36-50	43
51	29.608117	82.889117	122.91	212.91	36-50	43
52	29.598206	82.889408	111.17	201.17	21-35	28
53	29.612078	82.895883	294.92	24.92	36-50	43
54	29.604917	82.895817	120.33	210.33	36-50	43
55	29.607011	82.903711	301.14	31.14	36-50	43
56	29.672569	82.685294	109.72	199.72	51-65	58
57	29.667881	82.702097	76.98	166.98	51-65	58
58	29.672769	82.707099	73.42	163.42	51-65	58
59	29.656237	82.711671	83.92	173.92	51-65	58
60	29.641865	82.716398	90.00	180.00	6_20	13
61	29.681181	82.721184	67.38	157.38	51-65	58
62	29.667013	82.727572	118.25	208.25	21-35	28
63	29.653187	82.735125	72.14	162.14	6_20	13
65	29.690838	82.735840	88.13	178.13	6_20	13
66	29.653292	82.745308	73.17	163.17	21-35	28
67	29.659675	82.754575	75.03	165.03	21-35	28
68	29.657456	82.768818	79.08	169.08	36-50	43
69	29.685099	82.771694	87.22	177.22	6_20	13
70	29.687271	82.778841	88.48	178.48	6_20	13
71	29.697992	82.784909	80.78	170.78	6_20	13
72	29.682735	82.809655	114.94	204.94	21-35	28
73	29.700244	82.816804	111.68	201.68	6_20	13
74	29.718140	82.786701	306.09	36.09	6_20	13
75	29.713983	82.802763	90.00		0-5	2
77	29.661287	82.824372	97.43	187.43	21-35	28
78	29.681068	82.842062	100.71	190.71	6_20	13
79	29.682245	82.856095	104.21	194.21	6_20	13
80	29.672521	82.855779	89.07	179.07	21-35	28
81	29.663384	82.856227	109.58	199.58	36-50	43

Appendix B.1 Continued

Station	Latitude	Longitude	BedStrike	DipDirection	DipAngle	Avg Dip Angle
82	29.658430	82.856273	92.57	182.57	21-35	28
83	29.693325	82.887126	90.00		0-5	2
84	29.684728	82.941029	50.53	140.53	6_20	13
85	29.625551	82.796152	106.99	196.99	6_20	13
86	29.621661	82.796903	90.00		0-5	2
87	29.619018	82.798154	107.00	197.00	6_20	13
88	29.610951	82.798898	100.39	190.39	21-35	28
89	29.599842	82.808262	103.89	193.89	21-35	28
90	29.617464	82.807142	111.13	201.13	21-35	28
91	29.596018	82.812974	97.86	187.86	36-50	43
92	29.594533	82.816840	90.00		0-5	2
93	29.602240	82.820598	107.60	197.60	21-35	28
94	29.610451	82.822384	105.67	195.67	36-50	43
95	29.594628	82.827290	98.88	188.88	6_20	13
96	29.607103	82.835779	111.58	201.58	21-35	28
97	29.592301	82.835852	106.09	196.09	66-85	76
98	29.589870	82.839017	104.68	194.68	36-50	43
99	29.600407	82.840984	109.58	199.58	36-50	43
100	29.606911	82.841034	284.51	14.51	51-65	58
101	29.598911	82.845532	112.06	202.06	36-50	43
102	29.592006	82.848548	90.00		0-5	2
103	29.601951	82.850095	108.10	198.10	36-50	43
104	29.593864	82.886002	289.34	19.34	21-35	28
105	29.586484	82.888121	109.76	199.76	36-50	43
106	29.581328	82.888091	285.15	15.15	36-50	43
107	29.579091	82.904305	115.03	205.03	21-35	28
108	29.568418	82.909413	273.55	3.55	36-50	43
109	29.573488	82.915407	99.21	189.21	21-35	28
110	29.544988	82.917163	278.73	8.73	36-50	43
111	29.551397	82.917678	104.78	194.78	36-50	43
112	29.559947	82.920786	104.94	194.94	21-35	28
113	29.578014	82.923422	104.24	194.24	21-35	28
114	29.519397	82.723758	306.57	36.57	21-35	28
115	29.528911	82.726581	122.47	212.47	6_20	13
116	29.534386	82.738881	302.97	32.97	86-90	88
117	29.540558	82.741444	304.22	34.22	66-85	76
118	29.555403	82.742792	299.38	29.38	21-35	28
119	29.511864	82.753986	307.91	37.91	86-90	88
120	29.533567	82.760297	298.52	28.52	51-65	58

Appendix B.1 Continued

Station	Latitude	Longitude	BedStrike	DipDirection	DipAngle	Avg Dip Angle
121	29.562556	82.756978	296.85	26.85	21-35	28
122	29.565897	82.761542	90.00		0-5	2
123	29.568061	82.764992	113.33	203.33	21-35	28
124	29.573172	82.775528	305.15	35.15	21-35	28
125	29.574108	82.785853	103.39	193.39	36-50	43
126	29.595706	82.773053	128.51	218.51	6_20	13
127	29.579586	82.799947	109.44	199.44	36-50	43
128	29.612744	82.766522	119.75	209.75	6_20	13
129	29.542700	82.768647	295.24	25.24	36-50	43
130	29.547681	82.771136	301.66	31.66	21-35	28
131	29.538981	82.775625	279.50	9.50	36-50	43
132	29.534447	82.778931	283.13	13.13	66-85	76
133	29.532075	82.781347	55.65	145.65	6_20	13
134	29.527236	82.786067	305.92	35.92	21-35	28
135	29.544989	82.786869	313.85	43.85	6_20	13
136	29.541103	82.791717	321.77	51.77	21-35	28
137	29.531664	82.794169	60.42	150.42	21-35	28
138	29.546528	82.793122	90.00		0-5	2
139	29.554294	82.794189	90.00		0-5	2
140	29.528097	82.800167	90.00		0-5	2
141	29.532178	82.801986	1.63	91.63	6_20	13
142	29.565456	82.798536	128.44	218.44	6_20	13
143	29.550450	82.803183	90.00		0-5	2
144	29.547244	82.807169	90.00		0-5	2
145	29.544842	82.808217	116.57	206.57	6_20	13
146	29.520689	82.807789	333.62	63.62	21-35	28
147	29.531233	82.808358	87.67	177.67	21-35	28
148	29.540983	82.814647	108.93	198.93	36-50	43
149	29.537586	82.825506	107.39	197.39	36-50	43
150	29.554028	82.810403	105.05	195.05	21-35	28
151	29.558169	82.811242	102.08	192.08	21-35	28
152	29.556047	82.823381	119.02	209.02	36-50	43
153	29.570739	82.824300	127.98	217.98	36-50	43
154	29.565514	82.825900	303.84	33.84	86-90	88
156	29.560869	82.830347	308.77	38.77	36-50	43
158	29.540822	82.829822	105.92	195.92	6_20	13
159	29.536864	82.833028	103.24	193.24	21-35	28
160	29.537353	82.843347	108.26	198.26	21-35	28
161	29.540422	82.852794	117.12	207.12	21-35	28

Appendix B.1 Continued

Station	Latitude	Longitude	BedStrike	DipDirection	DipAngle	Avg Dip Angle
162	29.543600	82.864428	113.79	203.79	21-35	28
163	29.530767	82.863647	298.56	28.56	86-90	88
164	29.534508	82.869286	115.07	205.07	21-35	28
165	29.529681	82.869742	118.79	208.79	86-90	88
166	29.526069	82.871858	105.75	195.75	36-50	43
167	29.574328	82.821133	112.12	202.12	36-50	43
170	29.567283	82.830075	112.37	202.37	51-65	58
172	29.590022	82.825622	117.20	207.20	21-35	28
173	29.578086	82.825625	90.00		0-5	2
174	29.586131	82.830961	109.19	199.19	21-35	28
175	29.581358	82.837647	83.51	173.51	21-35	28
176	29.571022	82.842758	102.51	192.51	6_20	13
177	29.580833	82.844519	105.95	195.95	6_20	13
178	29.565156	82.852592	100.09	190.09	6_20	13
179	29.587144	82.854250	90.00		0-5	2
180	29.582631	82.855969	103.62	193.62	6_20	13
181	29.576342	82.858531	105.40	195.40	6_20	13
182	29.564736	82.869022	105.95	195.95	6_20	13
183	29.559372	82.876842	91.74	181.74	6_20	13
185	29.511156	82.809589	25.78	115.78	21-35	28
186	29.511103	82.820397	290.18	20.18	21-35	28
187	29.502300	82.828700	90.00		0-5	2
188	29.510381	82.827808	302.66	32.66	21-35	28
189	29.516172	82.830258	108.94	198.94	36-50	43
190	29.509139	82.831333	90.00		0-5	2
191	29.512272	82.832536	119.30	209.30	21-35	28
192	29.504508	82.838181	276.22	6.22	21-35	28
193	29.514611	82.836181	90.00		0-5	2
194	29.501039	82.843850	90.00		0-5	2
195	29.519203	82.835608	306.92	36.92	6_20	13
196	29.523606	82.834706	105.20	195.20	21-35	28
197	29.528886	82.832672	111.97	201.97	21-35	28
198	29.530317	82.843181	99.39	189.39	21-35	28
199	29.521514	82.851264	291.08	21.08	66-85	76
200	29.521953	82.860989	291.01	21.01	36-50	43
201	29.508981	82.858725	281.91	11.91	36-50	43
202	29.474708	82.829656	298.43	28.43	6_20	13
203	29.486206	82.835456	306.34	36.34	21-35	28
204	29.501878	82.850203	285.00	15.00	51-65	58

Appendix B.1 Continued

Station	Latitude	Longitude	BedStrike	DipDirection	DipAngle	Avg Dip Angle
205	29.501186	82.856944	278.07	8.07	36-50	43
206	29.503278	82.865444	273.92	3.92	66-85	76
207	29.499458	82.869672	279.36	9.36	66-85	76
208	29.505250	82.873667	275.38	5.38	36-50	43
209	29.490328	82.873733	90.00		0-5	2
210	29.483064	82.855522	90.00		0-5	2
211	29.488114	82.852956	307.69	37.69	86-90	88
212	29.462222	82.836053	305.31	35.31	36-50	43
213	29.491617	82.741869	304.94	34.94	51-65	58
214	29.487669	82.758664	308.48	38.48	36-50	43
215	29.445219	82.757194	64.22	154.22	6_20	13
216	29.450889	82.772514	132.39	222.39	51-65	58
217	29.438222	82.777122	82.97	172.97	6_20	13
218	29.454483	82.782233	298.94	28.94	51-65	58
219	29.476656	82.773700	313.29	43.29	66-85	76
220	29.489381	82.786117	90.00		0-5	2
221	29.462369	82.792356	300.36	30.36	66-85	76
222	29.498969	82.797419	317.34	47.34	36-50	43
223	29.437925	82.825472	308.94	38.94	36-50	43
224	29.448292	82.826803	313.79	43.79	36-50	43
227	29.424475	82.813942	128.30	218.30	21-35	28
228	29.414172	82.823739	115.27	205.27	66-85	76
229	29.423669	82.830944	128.87	218.87	36-50	43
230	29.327549	82.860614	302.19	32.19	36-50	43
231	29.332099	82.866408	303.73	33.73	36-50	43
232	29.340119	82.8687	311.55	41.55	36-50	43
233	29.346912	82.870988	131.28	221.28	36-50	43
234	29.358157	82.870017	312.62	42.62	36-50	43
235	29.364018	82.881352	0.21	90.21	36-50	43
236	29.372858	82.881696	318.31	48.31	36-50	43
237	29.380278	82.883364	325.33	55.33	66-85	76
238	29.384843	82.884264	327.23	57.23	66-85	76
239	29.388474	82.890575	310.68	40.68	66-85	76
240	29.391517	82.894414	90.00		0-5	2
241	29.395765	82.895486	297.02		85-90	88
242	29.410816	82.891302	57.03	147.03	21-35	28
243	29.421979	82.903669	325.76	55.76	21-35	28
244	29.461872	82.915812	308.97		85-90	88
245	29.471172	82.925158	311.26	41.26	51-65	58

Appendix B.1 Continued

Station	Latitude	Longitude	BedStrike	DipDirection	DipAngle	Avg Dip Angle
246	29.483597	82.930733	142.77	232.77	66-85	76
247	29.49255	82.942026	306.78	36.78	21-35	28
248	29.506583	82.938641	295.79	25.79	6-20.	13
249	29.522451	82.954241	298.4	28.4	21-35	28
250	29.532012	82.950669	115.27	205.27	36-50	43
251	29.489369	82.911573	270	180	0-5	2
252	29.502245	82.879803	109.04	199.04	36-50	43
253	29.496302	82.885492	289.68	19.68	21-35	28
254	29.486647	82.905436	294.36	24.36	6_20	13
255	29.487731	82.919518	137.72	227.72	36-50	43
256	29.502186	82.885768	296.93	26.93	66-85	76
257	29.493075	82.883945	284.72	14.72	21-35	28
258	29.48657	82.883465	295.32	25.32	21-35	28
259	29.487675	82.890106	297.19	27.19	21-35	28
260	29.479057	82.887859	123.55	213.55	21-35	28
261	29.478017	82.875657	311.69	41.69	21-35	28
262	29.464248	82.869821	305.08	35.08	36-50	43
263	29.513978	82.884336	124.05	214.05	21-35	28
264	29.510965	82.888455	122.64	212.64	36-50	43
265	29.515475	82.894575	116.09	206.09	36-50	43
266	29.519372	82.900392	127.18	217.18	21-35	28
267	29.527282	82.903071	147.88	237.88	6_20	13
268	29.529864	82.898472	306.06	36.06	21-35	28
269	29.511669	82.911878			0-5	2
270	29.51803	82.915782			0-5	2
271	29.520288	82.929375			0-5	2
272	29.492905	82.92103	100.6	190.6	66-85	76
273	29.48435	82.912556			0-5	2
274	29.463667	82.894244	302.75	32.75	36-50	43
275	29.451978	82.902637	309.24	39.24	36-50	43
276	29.448353	82.902625	301.01		85-90	88
277	29.446051	82.90331	311.75		85-90	88
278	29.434977	82.873808	307.95	37.95	21-35	28
279	29.449988	82.861947	298.09	28.09	36-50	43
280	29.443835	82.860949	310.8	40.8	21-35	28
281	29.438761	82.861249			0-5	2
282	29.430899	82.844284	321.52	51.52	51-65	58
283	29.406972	82.837402	117.33	207.33	66-85	76
284	29.399985	82.86569	123.61	213.61	66-85	76

Appendix B.1 Continued

Station	Latitude	Longitude	BedStrike	DipDirection	DipAngle	Avg Dip Angle
285	29.407185	82.817997	111.54	201.54	21-35	28
286	29.397778	82.824577	119.99	209.99	36-50	43
287	29.398165	82.846074	114.15	204.15	36-50	43
288	29.392063	82.86494	124.23	214.23	66-85	76
289	29.382776	82.869941	334.73	64.73	21-35	28
290	29.392187	82.847747	115.01	205.01	66-85	76
291	29.390179	82.856158	123.94	213.94	36-50	43
292	29.383425	82.860204	110.58	200.58	21-35	28
293	29.391888	82.840196	129.63	219.63	21-35	28
294	29.387444	82.844589	18.49	108.49	6_20	13
295	29.373646	82.87067	47.8	137.8	21-35	28
296	29.363991	82.881296	0.44	90.44	36-50	43
297	29.370053	82.866789	52.48	142.48	21-35	28
298	29.374771	82.847645	0.88	90.88	21-35	28
299	29.373401	82.839576	28.37	118.37	36-50	43
300	29.363217	82.862068	115.39	205.39	6_20	13
301	29.383787	82.831125	15.48	105.48	21-35	28
302	29.388083	82.805744	1.19	91.19	6_20	13
303	29.369964	82.823909	328.11	58.11	6_20	13
304	29.370799	82.817849			0-5	2
305	29.368793	82.814932	151.29	241.29	6_20	13
306	29.362522	82.827884	324.8	54.8	6_20	13
307	29.360942	82.814861	147.87	237.87	21-35	28
308	29.364446	82.804726	149.71	239.71	21-35	28
309	29.373616	82.8049	148.68	238.68	21-35	28
310	29.381153	82.795983	129.96	219.96	21-35	28
311	29.396137	82.762889	128.07	218.07	21-35	28
312	29.34911	82.838164	316.35	46.35	21-35	28
313	29.349699	82.851377	318.47	48.47	21-35	28
314	29.343105	82.844203	124.3	214.3	36-50	43
315	29.339304	82.852041	127.55	217.55	51-65	58
316	29.337237	82.85966	129.45	219.45	36-50	43
317	29.332194	82.866522	302.61	32.61	36-50	43
318	29.327787	82.860757	302.19	32.19	36-50	43
319	29.321171	82.875637	296.73	26.73	36-50	43
320	29.316866	82.886773	300.18	30.18	36-50	43
321	29.318282	82.891974	302.19	32.19	66-85	76
322	29.321654	82.895362	315.21	45.21	36-50	43
323	29.324818	82.897983	312.63	42.63	36-50	43

Appendix B.1 Continued

Station	Latitude	Longitude	BedStrike	DipDirection	DipAngle	Avg Dip Angle
324	29.324942	82.905107	314.65	44.65	36-50	43
325	29.314519	82.895646	134.36	224.36	21-35	28
326	29.309219	82.893491	133.71	223.71	36-50	43
327	29.311206	82.90484	310.88	40.88	36-50	43
328	29.315697	82.910908	313.07	43.07	36-50	43
329	29.304786	82.901867	310.15		85-90	88
330	29.300438	82.908925	315.82	45.82	36-50	43
331	29.317892	82.926218	317.13	47.13	36-50	43
332	29.305403	82.927865	320.39	50.39	21-35	28
333	29.303192	82.933512	319.89	49.89	21-35	28
334	29.284789	82.926925	320.65	50.65	36-50	43
335	29.280808	82.939073	318.93	48.93	51-65	58
336	29.28985	82.948743	320	50	36-50	43
337	29.289373	82.960669	321.6	51.6	36-50	43
338	29.273843	82.957354	309.09	39.09	36-50	43
339	29.357643	82.795741	132.09	222.09	6_20	13
340	29.338139	82.792379			0-5	2
341	29.332398	82.792089	322.28	52.28	51-65	58
342	29.345253	82.797863	145.02	235.02	21-35	28
343	29.338139	82.799022	129.28	219.28	21-35	28
344	29.327562	82.793059	324.27		85-90	88
345	29.324589	82.79869	317.2		36-50	43
346	29.32034	82.790456	325.01	55.01	36-50	43
347	29.322218	82.795108	139.38	229.38	36-50	43
348	29.332241	82.81018	131.83	221.83	6_20	13
349	29.34691	82.816588	135.38	225.38	36-50	43
350	29.34212	82.827021	116.72	206.72	21-35	28
351	29.322904	82.835425			0-5	2
352	29.312216	82.828538	135.62	225.62	66-85	76
353	29.30657	82.794376	314.31	44.31	36-50	43
354	29.30132	82.803464	317.69	47.69	36-50	43
355	29.294721	82.801723	317.07	47.07	66-85	76
356	29.29566	82.807391	320.94	50.94	66-85	76
357	29.320974	82.860238	123.04	213.04	36-50	43
358	29.299216	82.860282	105.5	195.5	6_20	13
359	29.297686	82.878291	122.53	212.53	6_20	13
360	29.293206	82.886573	315.27	45.27	6_20	13
361	29.300934	82.887595	312.17	42.17	66-85	76
362	29.297585	82.896959	312.13		85-90	88

Appendix B.1 Continued

Station	Latitude	Longitude	BedStrike	DipDirection	DipAngle	Avg Dip Angle
363	29.283998	82.892939	225.16	315.16	6_20	13
364	29.294245	82.903994	310.41	40.41	36-50	43
365	29.279779	82.873263	275.14	5.14	21-35	28
366	29.279836	82.880801	299.3		85-90	88
367	29.275365	82.88168	281.16	11.16	6_20	13
368	29.288083	82.825726	126.05	216.05	66-85	76
369	29.285221	82.825504	309.69	39.69	36-50	43
370	29.282509	82.819444	134.06	224.06	6_20	13
371	29.27604	82.821418	309.41	39.41	66-85	76
372	29.285292	82.837514	124.75	214.75	21-35	28
373	29.275	82.83206	308.88		85-90	88
374	29.277194	82.841374	123.47	213.47	6_20	13
375	29.27222	82.838874	312.47		85-90	88
376	29.267645	82.8376	316.07	46.07	66-85	76
377	29.280426	82.846873	126.46	216.46	36-50	43
378	29.272906	82.843517	311.47	41.47	36-50	43
379	29.275959	82.868885	302.9	32.9	66-85	76
380	29.267905	82.867597	129.16	219.16	6_20	13
381	29.265277	82.87721	125.01	215.01	6_20	13
382	29.25996	82.893193	130.51	220.51	6_20	13
383	29.273174	82.903541			0-5	2
384	29.266572	82.90081	315.82		86-90	88
385	29.275544	82.906992	338.98	68.98	36-50	43
386	29.27766	82.918086	336.69	66.69	66-85	76
387	29.264021	82.907583	305.82		86-90	88
388	29.260165	82.902557	317.09	47.09	66-85	76
389	29.245865	82.897196	312.97	42.97	66-85	76
390	29.24571	82.91539	140.79	230.79	66-85	76
391	29.246054	82.923926	309.87	39.87	21-35	28
392	29.245822	82.941161	325.29	55.29	21-35	28
393	29.236864	82.926533	311.11	41.11	36-50	43
394	29.238609	82.915653	137.32	227.32	36-50	43
395	29.234094	82.911136	127.65	217.65	66-85	76
396	29.224601	82.899242	316.86	46.86	21-35	28
397	29.227414	82.915745	317.99		86-90	88
398	29.219243	82.912819	319.07	49.07	36-50	43
399	29.225509	82.938146	306.11	36.11	36-50	43
400	29.216437	82.934246	142.82	232.82	51-65	58
401	29.219283	82.961456	294.61	24.61	6_20	13

Appendix B.1 Continued

Station	Latitude	Longitude	BedStrike	DipDirection	DipAngle	Avg Dip Angle
402	29.210715	82.956193	302.74	32.74	21-35	28
403	29.20818	82.97516	306.6	36.6	21-35	28
404	29.199832	82.941763	306.49		86-90	88
405	29.19372	82.931156	128.03	218.03	6_20	13
406	29.18403	82.930209			0-5	2
407	29.170432	82.915247	315.03	45.03	51-65	58
408	29.194329	82.96258	317.9	47.9	66-85	76
409	29.184029	82.960611			0-5	2
410	29.178799	82.947915			0-5	2
411	29.166534	82.964671			0-5	2
412	29.346686	82.859681	311.98	41.98	36-50	43
413	29.347298	82.866042	312.39	42.39	36-50	43
414	29.342407	82.875276	113.84	203.84	51-65	58
415	29.333629	82.87296	311.77	41.77	66-85	76
416	29.33434	82.876937	311.41		86-90	88
417	29.35088	82.886183	98.46	188.46	36-50	43
418	29.337844	82.890503	117.11	207.11	36-50	43
419	29.326567	82.890871	132.47	222.47	36-50	43
420	29.326043	82.888155	326.92	56.92	21-35	28
421	29.351409	82.905075	303.24		86-90	88
422	29.341984	82.924163	131.59	221.59	36-50	43
423	29.336881	82.931349	135.81	225.81	21-35	28
424	29.332126	82.920152	304.22	34.22	66-85	76
425	29.332175	82.929884	310.34	40.34	66-85	76
426	29.329505	82.925953	120.32	210.32	66-85	76
427	29.324073	82.93051	132.29	222.29	21-35	28
428	29.314422	82.933708	145.3	235.3	66-85	76
429	29.311018	82.939703	134.47	224.47	66-85	76
430	29.316324	82.95182	136.69	226.69	66-85	76
431	29.306087	82.95524	145.37	235.37	36-50	43
432	29.30495	82.947975	134.04	224.04	66-85	76
433	29.302894	82.945419	308.6		85-90	88
434	29.305263	82.964666	138.58	228.58	66-85	76
435	29.299554	82.964191	143.29	233.29	36-50	43
436	29.293792	82.973022	136.83	226.83	21-35	28
437	29.290089	82.972214	306.51	36.51	21-35	28
438	29.410436	82.8743	334.35	64.35	36-50	43
439	29.395266	82.884021	329.07	59.07	36-50	43
440	29.378441	82.890861	141.04	231.04	66-85	76

Appendix B.1 Continued

Station	Latitude	Longitude	BedStrike	DipDirection	DipAngle	Avg Dip Angle
441	29.367994	82.887227	321.09	51.09	36-50	43
442	29.375257	82.898454	323.05	53.05	66-85	76
443	29.370085	82.905262	142.88	232.88	36-50	43
444	29.36685	82.898277	152.51	242.51	21-35	28
445	29.367671	82.91089	137.39	227.39	36-50	43
446	29.362316	82.898539	317.96	47.96	36-50	43
447	29.357977	82.900859	132.31	222.31	66-85	76
448	29.358659	82.9104	127.42	217.42	66-85	76
449	29.356413	82.90798	310.68		86-90	88
450	29.352815	82.91423	126.79	216.79	6_20	13
451	29.349974	82.912637	303.19	33.19	36-50	43
452	29.349037	82.916756	306.38		86-90	88
453	29.346991	82.921133	129.97	219.97	36-50	43
454	29.350371	82.931573	118.37	208.37	21-35	28
455	29.354815	82.934477	113.7	203.7	36-50	43
456	29.336782	82.942539	138.5	228.5	36-50	43
457	29.335654	82.941139	319.54	49.54	66-85	76
458	29.329862	82.944031	319.02		86-90	88
459	29.336963	82.949805	142.96	232.96	21-35	28
460	29.328241	82.948874	333.48	63.48	36-50	43
461	29.334219	82.96051	127.76	217.76	36-50	43
462	29.328727	82.956006	131.22	221.22	36-50	43
463	29.323218	82.957603	320.03	50.03	36-50	43
464	29.320105	82.957054	312.52		86-90	88
465	29.326166	82.969798	146.61	236.61	36-50	43
466	29.318915	82.962012	316.56	46.56	36-50	43
467	29.315918	82.95955	313.71	43.71	66-85	76
468	29.312944	82.965803	315.12	45.12	21-35	28
469	29.310483	82.962714	139.02	229.02	66-85	76
470	29.312185	82.974041	119.7	209.7	21-35	28
471	29.319056	82.980136	313.96	43.96	36-50	43
472	29.315977	82.978576	132.68	222.68	66-85	76
473	29.311521	82.980416	128.35	218.35	66-85	76
474	29.308292	82.97364	312.28	42.28	36-50	43
475	29.307778	82.980751	318.33		86-90	88
476	29.302418	82.98102	317.74	47.74	66-85	76
477	29.308848	82.991537	312.17	42.17	66-85	76
478	29.304944	82.994289	130.41	220.41	6_20	13
479	29.301979	82.992196	303.38	33.38	66-85	76

Appendix B.1 Continued

Station	Latitude	Longitude	BedStrike	DipDirection	DipAngle	Avg Dip Angle
480	29.305812	82.999801	129.2	219.2	6_20	13
481	29.29261	82.985623	324.4		86-90	88
482	29.290512	82.984477	318.73	48.73	66-85	76
483	29.291302	82.980343	320.67	50.67	36-50	43
484	29.291907	82.002966	317.51	47.51	36-50	43
485	29.293778	82.005266	318.25	48.25	36-50	43
486	29.279939	82.990019	328.12	58.12	6_20	13
487	29.28211	82.995056	321.48		86-90	88
488	29.281644	83.001129	317.75	47.75	51-65	58
489	29.265076	83.01964	316.89	46.89	36-50	43
490	29.251807	83.033146	319.99	49.99	36-50	43
491	29.383921	82.900892	142.01	232.01	36-50	43
492	29.380798	82.917543	132.62	222.62	6_20	13
493	29.382378	82.920144	319.47	49.47	66-85	76
494	29.375789	82.917376	130.13	220.13	6_20	13
495	29.373104	82.931637	121.05	211.05	21-35	28
496	29.363954	82.930249	81.77	171.77	21-35	28
497	29.261303	82.924357			0-5	2
498	29.401119	82.913903	112.65	202.65	21-35	28
499	29.402759	82.92183	122.17	212.17	36-50	43
500	29.395042	82.920189	132.01	222.01	6_20	13
501	29.404783	82.925797	313.27	43.27	66-85	76
502	29.396314	82.930233	133.71	223.71	36-50	43
503	29.41161	82.930354	328.31	58.31	21-35	28
504	29.417017	82.93628	1.85	91.85	6_20	13
505	29.400716	82.940882	301.78	31.78	6_20	13
506	29.387612	82.943922	126.11	216.11	66-85	76
507	29.39436	82.949676	322.7	52.7	36-50	43
508	29.386874	82.961933	306.99	36.99	21-35	28
509	29.37912	82.949852	125.8	215.8	66-85	76
510	29.379548	82.968835	45.43	135.43	6_20	13
511	29.375085	82.955878	292.92	22.92	66-85	76
512	29.372091	82.959953	107.33	197.33	66-85	76
513	29.365669	82.968977	119.9	209.9	6_20	13
514	29.359759	82.962687	135.45	225.45	6_20	13
515	29.297129	83.070057	307.99	37.99	21-35	28
516	29.311409	83.075454	311.36	41.36	36-50	43
517	29.302	83.088772	286.78	16.78	21-35	28
518	29.301359	83.100892	291.24	21.24	36-50	43

Appendix B.1 Continued

Station	Latitude	Longitude	BedStrike	DipDirection	DipAngle	Avg Dip Angle
519	29.338298	83.117734			0-5	2
520	29.333732	83.136887	324.24	54.24	6_20	13
521	29.355719	83.129195	320.56	50.56	36-50	43
522	29.357792	83.138457	314.13	44.13	21-35	28
523	29.373045	83.159077	325.17	55.17	21-35	28
524	29.405241	83.134735			0-5	2
525	29.410591	83.135664	147.3	237.3	51-65	58
526	29.410953	83.16277	302.39	32.39	6_20	13
527	29.432376	83.169948			0-5	2
528	29.43116	83.17211	129.76	219.76	6_20	13
529	29.427135	83.087457	320.15	50.15	21-35	28
530	29.454604	83.100359	322.33	52.33	21-35	28
531	29.445163	83.180719	124.35	214.35	51-65	58
532	29.45282	83.186501	140.86	230.86	36-50	43
533	29.461201	83.193776	124.31	214.31	21-35	28
534	29.472014	83.210765	138.06	228.06	21-35	28
535	29.360485	82.942374	135.6	225.6	36-50	43
536	29.364349	82.943039	110.61	200.61	21-35	28
537	29.37077	82.942385	135.62	225.62	6_20	13
538	29.355845	82.948007	131.47	221.47	6_20	13
539	29.354014	82.960654	135.59	225.59	6_20	13
540	29.342657	82.990663	108.1	198.1	36-50	43
541	29.352054	82.983112	108.8	198.8	21-35	28
542	29.358824	82.978718	128.28	218.28	21-35	28
543	29.361253	82.985483	308.8	38.8	36-50	43
544	29.369077	82.980002	302.22	32.22	66-85	76
545	29.366313	82.975609	81.09	171.09	6_20	13
546	29.356374	82.994086	312.02	42.02	66-85	76
547	29.352707	82.002573	292.17	22.17	66-85	76
548	29.376184	82.989988			0-5	2
549	29.379054	82.989834	321.44	51.44	6_20	13
550	29.387701	82.98245	297.67	27.67	6_20	13
551	29.391561	82.986165	309.95	39.95	6_20	13
552	29.388184	82.967543	318.92	48.92	36-50	43
553	29.41144	82.964395	311.88	41.88	6_20	13
554	29.403087	82.956079	310.83	40.83	36-50	43
555	29.416724	82.943826	330.98	60.98	36-50	43
556	29.420499	82.953519	302.24	32.24	36-50	43
557	29.422879	82.939981	327.53	57.53	51-65	58

Appendix B.1 Continued

Station	Latitude	Longitude	BedStrike	DipDirection	DipAngle	Avg Dip Angle
558	29.43108	82.957293	315.94	45.94	6_20	13
559	29.43685	82.945644	303.99	33.99	36-50	43
560	29.428826	82.936202	315	45	66-86	76
561	29.427667	82.919291	126.1	216.1	66-85	76
562	29.429331	82.922818	311.3	41.3	36-50	43
563	29.43248	82.92317	308.47	38.47	21-35	28
564	29.437499	82.931989	299	29	36-50	43
565	29.44556	82.961428	121.53	211.53	36-50	43
566	29.482337	82.936254	147.29	237.29	36-50	43
567	29.49177	82.953834	121.97	211.97	21-35	28
568	29.494985	82.954087	115	205	6_20	13
569	29.495177	82.950573	292.82	22.82	6_20	13
570	29.49843	82.949323	116.84	206.84	36-50	43
571	29.500402	82.949429	293.61	23.61	21-35	28
572	29.500586	82.946399	302.48	32.48	6_20	13
573	29.502643	82.943279	271.2	1.2	6_20	13
574	29.514237	82.961675	298.28	28.28	36-50	43
575	29.501019	82.964155			0-5	2
576	29.494478	82.964426	307.12	37.12	51-65	58
577	29.497774	82.971056	303.38	33.38	21-35	28
578	29.490244	82.979597	302.75	32.75	21-35	28
579	29.498166	82.984368	299.11	29.11	66-85	76
580	29.500247	82.984788	318.06	48.06	6_20	13
581	29.505593	82.990369	106.08	196.08	21-35	28
582	29.500856	82.006357	313.25	43.25	21-35	28
583	29.492009	82.010822	318.29	48.29	21-35	28
584	29.498527	83.024229	314.68	44.68	21-35	28
585	29.482091	83.015074	117.68	207.68	36-50	43
586	29.489676	83.03012	47.46	137.46	6_20	13
587	29.472109	83.018906	127.24	217.24	36-50	43
588	29.474306	83.020132	285.64		85-90	88
589	29.485686	83.040154	103.26	193.26	21-35	28
590	29.481223	83.039068	286.17	16.17	6_20	13
591	29.480126	83.036338	110.38	200.38	21-35	28
592	29.471166	83.026526			0-5	2
593	29.468863	83.026259	275.27		86-90	88
594	29.47256	83.035725	293.08	23.08	21-35	28
595	29.467966	83.043616	298.4	28.4	21-35	28
596	29.462897	82.997563			0-5	2

Appendix B.1 Continued

Station	Latitude	Longitude	BedStrike	DipDirection	DipAngle	Avg Dip Angle
597	29.459785	82.977395	140.34	230.34	6_20	13
598	29.453938	82.986483	89.38	179.38	6_20	13
599	29.453416	82.998511	5.61	95.61	36-50	43
600	29.457271	83.000939	135.03	225.03	36-50	43
601	29.459848	83.002491	243.18	333.18	6_20	13
602	29.448301	82.992176	266.54	356.54	6_20	13
603	29.448109	82.002902	337.98	67.98	21-35	28
604	29.450584	83.009314			0-5	2
605	29.442874	82.995638	288.32	18.32	6_20	13
606	29.440531	82.003801			0-5	2
607	29.435523	83.000572	136.13	226.13	21-35	28
608	29.435085	82.99422	117.61	207.61	21-35	28
609	29.432924	82.991179			0-5	2
610	29.426997	82.997305	244.23	334.23	6_20	13
611	29.420102	82.993359	316.84	46.84	6_20	13
612	29.438363	83.012306			0-5	2
613	29.432807	83.019672	319	49	6_20	13
614	29.444469	83.008733			0-5	2
615	29.447207	83.01425			0-5	2
616	29.473833	83.083112	351.51	81.51	6_20	13
617	29.476368	83.069219	111.57	201.57	36-50	43
618	29.479661	83.07223	28.11	118.11	21-35	28
619	29.48249	83.074342	323.63	53.63	21-35	28
620	29.489395	83.063774	303.97	33.97	21-35	28
621	29.493761	83.067903	122.87	212.87	21-35	28
622	29.490237	83.0754	37.4	127.4	6_20	13
623	29.393499	83.061292	307.29		86-90	88
624	29.500839	83.061861	114.34	204.34	21-35	28
625	29.502518	83.073701	118.48	208.48	66-85	76
626	29.491006	83.083603	303.73		86-90	88
627	29.492972	83.096069	240.49	330.49	36-50	43
628	29.509537	83.062728	288.46	18.46	21-35	28
629	29.508107	83.067666	296.1		86-90	88
630	29.511368	83.070948	111.04	201.04	66-85	76
631	29.50228	83.083358	111.13	201.13	51-65	58
632	29.512547	83.080395	102.61	192.61	66-85	76
633	29.505087	83.093672	117.53	207.53	51-65	58
634	29.507676	83.099408	112.09	202.09	36-50	43
635	29.501324	83.112845	119.37	209.37	66-85	76

Appendix B.1 Continued

Station	Latitude	Longitude	BedStrike	DipDirection	DipAngle	Avg Dip Angle
636	29.495125	83.10767	122.86	212.86	36-50	43
637	29.497088	83.122891	119.86	209.86	51-65	58
638	29.49919	83.132934	123.52	213.52	36-50	43
639	29.517423	83.112964	90.55	180.55	21-35	28
640	29.528117	83.122851	119.96	209.96	66-85	76
641	29.182	83.125277	105.82	195.82	66-85	76
642	29.553907	83.146878	105.27	195.27	36-50	43
643	29.538665	83.115239	102.53	192.53	21-35	28
644	29.53534	83.104243	107.27	197.27	21-35	28
645	29.529831	83.088656	100.87	190.87	21-35	28
646	29.540552	83.086338	103.72	193.72	21-35	28
647	29.520812	83.069481	113.05	203.05	66-85	76
648	29.516165	83.065205	275.88		86-90	88
649	29.513111	83.060531	276.76	6.76	6_20	13
650	29.531981	83.055155	101.74	191.74	6_20	13
651	29.548854	83.053628	107.52	197.52	21-35	28
652	29.563629	83.064822	106.9	196.9	21-35	28
653	29.555586	83.084968	84.15	174.15	6_20	13
654	29.561879	83.081104	85.22	175.22	6_20	13
655	29.56928	83.081356	100.29	190.29	21-35	28
656	29.576184	83.083306	101.63	191.63	36-50	43
657	29.579912	83.083284	104.62	194.62	66-85	76

Appendix B.2

Stutz Strike and Dip Measurements

Station	Latitude	Longitude	StrikeAzimuth	DipDirection	DipAngle
1	29.625947	82.606528	280.28	190.28	80
2	29.621687	82.607544	279.57	9.57	90
3	29.632371	82.603958	281.17	11.17	88
4	29.642941	82.600484	304.71	34.71	37
5	29.618206	82.560907	286.41	16.41	75
6	29.619504	82.568367	301.12	211.12	61
8	29.605968	82.557042	303.45	33.45	75
9	29.61748	82.578872	287.89	197.89	76
10	29.605332	82.589649	295.43	205.43	84
11	29.586029	82.583877	288.21	18.21	78
12	29.597189	82.573142	298.92	28.92	60
13	29.57105	82.61132	275.58	185.58	34
14	29.622714	82.724897	305.88	215.88	75
15	29.589011	82.65621	329.98	239.98	88
16	29.651488	82.647707	284.16	14.16	85
17	29.606051	82.660064	86.35	176.35	76
18	29.594628	82.66585	325.71	55.71	25
19	29.574772	82.677861	274.87	184.87	76
20	29.5999	82.718546	305.36	215.36	84
21	29.562384	82.672647	307.4	37.4	75
22	29.526093	82.755797	279.63	9.63	64
23	29.505088	82.703881	302.16	32.16	81
24	29.481099	82.796438	311.69	221.69	89
25	29.588275	82.826567	296.16	26.16	90
26	29.66011	82.67822	291.88	21.88	59
27	29.568925	82.930513	301.38	211.38	59
28	29.503618	82.868906	283.69	13.69	47
29	29.558044	82.80801	270.45	180.45	41
30	29.555423	82.823418	324.22	54.22	85

Appendix B.2 continued

Station	Latitude	Longitude	StrikeAzimuth	DipDirection	DipAngle
31	29.634215	82.670905	288.97	198.97	67
32	29.485845	82.917843	323.35	233.35	90
33	29.517987	82.838427	285.01	15.01	64
34	29.581464	82.894681	299.19	209.19	67
35	29.499164	82.724727	305.05	35.05	85
36	29.492262	82.739532	281.58	11.58	77
37	29.47559	82.744325	330.52	240.52	85
38	29.468932	82.748172	289.59	19.59	79
39	29.593197	82.554939	272.77	182.77	71
40	29.660039	82.863583	315.42	225.42	83
41	29.486313	82.760841	284	14	76

Appendix C

Appendix C.1 Strike and Dip of THS Fold Limbs

The following strike and dip measurements describe the orientations of folds, primarily synclines, within the respective cross sections. Measurements are given for each syncline as it is predicted to have been oriented pre-STD folding as well a their current post-STD measurements.

A-A' pre-STD folding

limb	strike	dip direction	dip angle
1: SW limb	290	20	31
2: NE limb	290	200	40
2: SW limb	290	20	12
2: NE limb	290	200	35

A-A' post-STD folding

limb	strike	dip direction	dip angle
1: SW limb	290	20	51
1: NE limb	290	200	42
2: SW limb	290	20	11
2: NE limb	290	200	53

B-B' pre-STD folding

limb	strike	dip direction	dip angle
1: SW limb	335	65	6
1: NE limb	335	245	14
2: SW limb	335	65	27
2: NE limb	335	245	19
3: SW limb	312	42	33
3: NE limb	312	222	30
4: SW limb	312	42	46
4: NE limb	312	222	16
5: SE limb	312	42	57
5: NW limb	312	222	27

B-B' post-STD folding

limb	strike	dip direction	dip angle
1: SW limb	335	65	68
1: NE limb	335	245	20
2: SW limb	335	65	34
2: NE limb	335	245	8
3: SW limb	312	42	25
3: NE limb	312	222	35
4: SW limb	312	42	38
4: NE limb	312	222	23
5: SE limb	312	42	44
5: NW limb	312	222	42

C-C' pre-STD folding

limb	strike	dip direction	dip angle
1: SW limb	304	34	27
1: NE limb	304	214	40
2: SW limb	304	34	11
2: NE limb	304	214	20
3: SW limb	304	34	21
3: NE limb	304	214	3

C-C' post-STD folding

limb	strike	dip direction	dip angle
1: SW limb	304	34	35
1: NE limb	304	214	30
2: SW limb	304	34	14
2: NE limb	304	214	22
3: SW limb	304	34	9
3: NE limb	304	214	25

D-D' pre-STD folding

limb	strike	dip direction	dip angle
1: NW limb	14	104	26
1: SE limb	14	284	28

D-D' post-STD folding

limb	strike	dip direction	dip angle
1: NW limb	14	104	38
1: SE limb	14	284	17

Appendix C.2 Dip and Plunge of THS Fold Limbs

The dip and plunge data for folds in each respective cross section are listed in the table below.

Axial Planes pre-STD Folding			**Axial Planes post-STD folding**		
A-A'	Dip	Plunge	A-A'	Dip	Plunge
1	85	0	1	86	12
2	78	0	2	69	12

B-B'	Dip	Plunge	B-B'	Dip	Plunge
1	85	0	1	66	0
2	86	0	2	77	0
3	89	0	3	85	0
4	75	0	4	82	0
5	75	0	5	89	0

C-C'	Dip	Plunge	C-C'	Dip	Plunge
1	84	0	1	87	0
2	85	0	2	86	4
3	81	0	3	82	0

D-D'	Dip	Plunge	D-D'	Dip	Plunge
1	89	0	1	79	0

7. REFERENCES

Achache J., V. Courtillot, and Y. Xiu, 1984, Paleogeographic and tectonic evolution of southern Tibet since middle Cretaceous time: New paleomagnetic data and synthesis, Journal of Geophysical Research, 89, 10311-10339.

Aikman, A.B., Harrison, T.M., and Lin, D., 2008, Evidence for early (>44 Ma) Himalaya crustal thickening, Tethyan Himalaya, southeastern Tibet: Earth and Planetary Science Letters, v. 274, p. 14-23.

Allison, David T., accessed Jan 2011, Three-Point Problem Solver, http://www.usouthal.edu/geography/allison/GY403/StructureSpreadsheets.htm.

Aoya, M., Wallis, S.R., Terada, K., Lee, J., Kawakami, T., Wang, Y., and Heizler, M., 2005, North-south extension in the Tibetan crust triggered by granite emplacement: Geology, v. 33, p. 853-856.

Beaumont, C. Jamieson, R.A., Nguyen, M.H., and Lee, B., 2001, Himalayan tectonics Explained by extrusion of a low-viscosity crustal channel coupled to focused surface denudation. Nature, 414: 738-742.

Beaumont, C., Jamieson, R.A., Nguyen, M.G., and Medvedev, S., 2004, Crustal channel flows: 1, Numerical models with applications to the tectonics of the Himalayan-Tibetan orogen: Journal of Geophysical Research, v. 109, p. B06406.

Beaumont, C., M. H. Nguyen, R. A. Jamieson, and S. Ellis, 2006, Crustal flow modes in large hot orogens, in *Channel Flow, Ductile Extrusion and Exhumation in Continental Collisional Zones*, edited by R. D. Law, M. P. Searle, and L. Godin, Geological Society, London, Special Publication 268, 91-146.

Besse, J., and V. Courtillot, 1988, Paleogeographic maps of the continents bordering the Indian Ocean since the Early Jurassic, Journal of Geophysical Research, 93, 11791-11808.

Besse, J., V. Courtillot, J.P. Pozzi, M. Westphal, and Y.X. Zhou, 1984, Palaeomagnetic estimates of crustal shortening in the Himalayan thrusts and Zangbo Suture, Nature, 311, 621-626.

Bird, P. 1991. Lateral extrusion of the lower crust from under high topography, in the isostatic limit. Journal of Geophysical Research, B, Solid Earth and Planets, 96: 10,275-10, 286.

Burchfiel, B.C., C. Zhiliang, K.V. Hodges, L. Yuping, L.H. Royden, D. Changron, and X. Jiene, 1992, The South Tibetan detachment system, Himalayan orogen: Extension contemporaneous with and parallel to shortening in a collisional mountain belt, Special Papers of the Geological Society of America, 269, pp. 51.

Burchfiel, B. C., and Royden, L. H., 1985, North-south extension within the convergent Himalayan region. Geology 13:679–682.

Colchen, M., Le Fort, P., and Pecher, A., 1981, Geological map of Annapurnas-Manaslu-Ganseh Himalaya, Nepal, in Gupta, H.K., and Delany, F.M., eds., Zagros-Hindu Kush-Himalaya geodynamic evolution: Washington D.C., American Geophysical Union, scale 1:200,000.

Coleman, M.E., and Hodges, K.V., 1995, Evidence for Tibetan plateau uplift before 14 myr ago from a new minimum age for east-west extension: Nature, v. 374, p. 49-52.

Coward M.P., and R.W.H. Butler, 1985, Thrust tectonics and the deep structure of the Paksitan Himalaya, Geology, 13, 417-420.

Davis, G.H., and Reynolds, S.J., 1996, Structural Geology of Rocks and Regions (2nd Edition): New Yrok, John Wiley and Sons, Inc.

Decelles, P. G., G. E. Gehrels, J. Quade, T. P Ojha, P. A. Kapp, B. N. Upreti, 1998, Neogene foreland basin deposits, erosional unroofing, and the kinematic history of the Himalayan fold-thrust belt, western Nepal, GSA Bulletin, v. 110, no. 1, p. 2-21.

Fuchs, G.: Beitrag zur Kenntnis des Palaozoikums und Mesozoikums der Tibetishen Zone in Dolpo (Nepal Himalaya), 1964, Verhandl Geol. Bundesanst., 6-15.

Fuchs, G., 1973, Geological Map of Western Dolpo, scale 1:80,000, published by Geologische Bundesanstalt, Wien.

Fuchs, G., The Geology of the Karnali and Dolpo Regions, Western Nepal, 1977, 165-217, Jahrb, Geol. B.-A., Band 120, Heft 2, Wien, Dezember.

Garzanti, E., Stratigraphy and sedimentary history of the Nepal Tethyan Himalaya passive margin, 1999, Journal of Asian Earth Sciences, v. 17, issue 5-6, p. 805-827.

Garzioni, C.N., DeCelles, P.G., Ojha, T.P., and Upreti, B.N., 2003, East-west extension and Miocene environmental change in the southern Tibetan plateau: Thakkhola graben, central Nepal: Geological Society of America Bulletin, v. 115, p. 3-20.

GeoEye Inc., 2011, GeoEye-1 Fact Sheet, http://launch.geoeye.com/LaunchSite/about/fact_sheet.aspx

Grujic,D., Casey,M.,Davidson, C.,Hollister, L. S.,Kündig, R., Pavlis, T., and Schmid, S., 1996, Ductile extrusion of the Higher Himalayan crystalline in Bhutan: Evidence from quartz microfabrics: Tectonophysics, v. 260, p. 21–43.

Godin, L., Parrish, R.R., Brown, R.D., and Hodges, K.V., 2001, Crustal thickening leading to exhumation of the Himalayan metamorphic core of central Nepal; insight from U-Pb geochronology and 40Ar/39Ar thermochronology: Tectonics, v. 20, p. 729-747, doi: 10.1029/2000TC001204.

Godin, L., Brown, R.L., Hanmer, S., and Parrish, R.R., 1999, Back folds in the core of the Himalayan orogen: An alternative interpretation: Geology, v. 27, p. 151-154.

Godin, L., Gleeson, T., Searle, M.P., Ullrich, T.D., and Parrish, R.R., 2006, Locking of southward extrusion in favour of rapid crustal-scale buckling of the Greater Himalayan sequence, Nar valley, central Nepal, in Law, R.D., Searle, M.P., and Godin, L., eds. Channel Flow, Ductile Extrusion in Continental Collision Zones: Geological Society of London Special Publication 268, p. 269-292.

Gleeson, T. P., Godin, L., 2006, The Chako antiform: A folded segment of the Greater Himalayan sequence, Nar valley, Central Nepal Hiamalay. Journal of Asien Earth Sciences, 27, 717-734

Harrison,T. M., Grove, M., McKeegan, K. D., Coath, C.D., Lovera, O. M. and Le Fort, P., 1999, Origin and episodic emplacement of the Manaslu intrusive complex, central Himalaya. Journal of Petrology, 40, 3–19.

Hodges, K.V., Tectonics of the Himalaya and southern Tibet from two perspectives, 2000, Geological Society of America Bulletin, 112, 324-350.

Hurtado, Jose, Chatterjee, Nilanjan, Ramezani, Jahandar, Hodges, Kip, and Bowring, Samuel, 2007, Electron Microprobe Chemical Dating of Uraninite as a Reconnaissance Tool for Leucogranite Geochronology. Available from Nature Precedings, http://hdl.handle.net/10101/npre.2007.655.1.

Jamieson, R. A., C. Beaumont, S. Medvedev, and M. H. Nguyen, 2004, Crustal channel flow: 2. Numerical models with implications for metamorphism in the Himalayan-Tibetan orogen*, Journal of Geophysical Research, 109*, doi: 10.1029/2003JB002811.

Kellet, D.A., and Godin, L., 2009, Pre-Miocene deformation of the Himalayan superstructure, Hidden valley, central Nepal: Journal of the Geological Society of London, v. 166, p. 261-275. doi:10.1144/0016-76492008-097.

Kohn, M. J., 2008, P-T-t data from central Nepal support critical taper and repudiate large-scale channel flow of the Greater Himalayan Sequence, Geological Society of America Bulletin, 120, 259-273.

Larson, K.P., Godin, L., and Price, R.A., 2010, Relationship between displacement and distortion in orogens: Linking the Himalayan foreland and hinterland in central Nepal: Geological Society of America Bulletin, v. 122, p. 1116-1134; doi: 10.1130/B30073.1.

Lefort, P., 1975, Himalayas: The collided range: Present knowledge of the continental arc, American Journal of Science, 275, 1-44.

Lee, J., Hacker, B., R., Dinklage, W. S., Wang, Y., Gans, P., Calvert, A., Wan, J., Chen, W., Blythe, A. E., and McClelland, W., 2000, Evolution of the Kangmar Dome, southern Tibet: Structural, petrologic, and thermochronologic constraints: Tectonics, v. 19, p. 872-895

Lee, J., and Whitehouse, M.J., 2007, Onset of mid-crustal extensional flow in southern Tibet: Geology, v. 35, p. 45-48; doi: 10.1130/G22842A.1.

Le Pichon, X., M. Fournier, and L. Jolivet, Kinematics, 1992, topography, shortening, and extrusion in the India-Eurasia collision, Tectonics, 11, 1985-1098.

Martin, A.J., P.G. DeCelles, G.E. Gehrels, P.J. Patchett, C. Isachsen, 2005, Isotopic and structural contraints on the location of the Main Central thrust in the Annapurna Range, Central Nepal Himalaya, Geological Society of America Bulletin, v. 117 no. 7/8, 926-944.

Murphy, M.A., and A. Yin, 2003, Structural evolution and sequence of thrusting in the Tethyan fold-thrust belt and Indus-Yalu suture zone, southwest Tibet, Geological Soceity of America Bulletin, 115, 21-34.

Murphy, M.A., 2007, Isotopic characteristics of the Gurla Mandata metamorphic core complex: Implications for the architecture of the Himalayan orogen. Geology, 35, 983-986.

Murphy, 2011, (personal communication)

Patriat, P., and J. Achache, 1984, Indian-Asia collision chronology has implication for crutal shortening and driving mechanisms of plates, Nature, 311, 615-621.

Price, R.A., 1986, The southeastern Canadian Cordillera: Thrust faulting, tectonic wedging, and delamination of the lithosphere: Journal of Structural Geology, v. 8, p. 239–254.

Robinson, D.M., P. G. DeCelles, and P. Copeland, 2006, Tectonic Evolution of the Himalayan Thrust Belt in western Nepal: Implications for channel flow models, Geological Society of America Bulletin, 118, 865-885.

Schelling, D., 1992, The Tectonostratigraphy and structure of the eastern Nepal Himalaya, Tectonics, 11, 925-943.

Schneider, C., and Masch, L., 1993, The metamorphism of the Tibetan Series from the Manang area, Marsyandi Valley, central Nepal, *in* Treloar, P. J., and Searle, M. P., eds., Himalayan tectonics: Geological Society (London) Special Publication 74, p. 357–374.

Searle, Michael P. and Godin, Laurent, 2003,"The South Tibetan Detachment and the Manaslu Leucogranite: A Structural Reinterpretation and Restoration of the Annapurna-Manaslu Himalaya, Nepal. Journal of Geology, vol. 111, p. 505-523.

Searle, M. P., and Rex, A. J., 1989, Thermal model for the Zanskar Himalaya. J. Metamorph. Geol. 7:127–134.

Searle, M. P.; Waters, D. J.; Dransfield, M. W.; Stephenson, B. J.; Walker, C. B.; Walker, J. D.; and Rex, D. C., 1999, Thermal and mechanical models for the structural evolution of Zanskar High Himalaya. *In* MacNiocaill, C., and Ryan, P. D., eds. Continental Tectonics. Geol. Soc. Lond. Spec. Publ. 164:139–156.

Srivastava, P. and G. Mitra, 1994, Thrust geometries and deep structure of the outer and lesser Himalaya, Kumaon and Garhwal (India): Implications for evolution of the Himalayan fold-and-thrust belt, Tectonics, 13, 89-109.

Webb, A. A. G., A. Yin, M. Harrison, J. Celerier, and W. Burgess, 2007, The leading edge of the Greater Himalayan Crystalline complex revealed in the NW Indian Himalaya: Implications for the evolution of the Himalayan orogen*, Geology, 35*, 955-958.

Weismayr, G. & Grasemann, B., 2002. Eohimalayan fold and thrust belt: for the geodynamic evolution of the NW-Himalaya (India). Tectonics, 21, 1058. DOI: 10/1029/2002TC001363.

Yin, A., 2006, Cenozoic tectonic evolution of the Himalayan orogen as constrained by along-strike variation of structural geometry, exhumation history, and foreland sedimentation: Earth-Science Reviews, v. 76, p. 1–131.